Real-Time Crystallization of $LiCoO_2$ from β-$Co(OH)_2$ and Co_3O_4: Synthetic Pathways and Structural Evolution

Marie Duffiet, Damian Goonetilleke, François Fauth, Torsten Brezesinski, Jürgen Janek, and Matteo Bianchini*

ABSTRACT: Cobalt oxides are technologically important materials, especially when lithiated for application as Li-ion cathodes. However, several phases may crystallize during solid-state synthesis in the Li−Co−O−H system. The solid-state reactions of $LiOH·H_2O$ with both β-$Co(OH)_2$ and Co_3O_4 have been investigated here through the combined use of high-resolution *in situ* synchrotron X-ray diffraction (XRD) and Raman spectroscopy, with a special focus on the low-temperature range (RT−600 °C). We show that several spinel phases (AB_2O_4 and $A_2B_2O_4$ with A, B = Li, Co) are formed in the range 300−525 °C, whose unambiguous identification is only possible through the complementary use of Raman spectroscopy as their XRD patterns are almost identical. While the various structures evidenced are mostly stabilized over similar temperature ranges regardless of the initial choice of Co precursor, the lithiated spinel phases are observed at lower temperatures for samples synthesized from $Co(OH)_2$. Moreover, their respective Li and Co fractions and crystallinity are strongly affected by the initial choice of precursor. These findings have strong implications in the preparation and optimization of both Co-based cathode active materials and Co-based coatings for other cathode active materials.

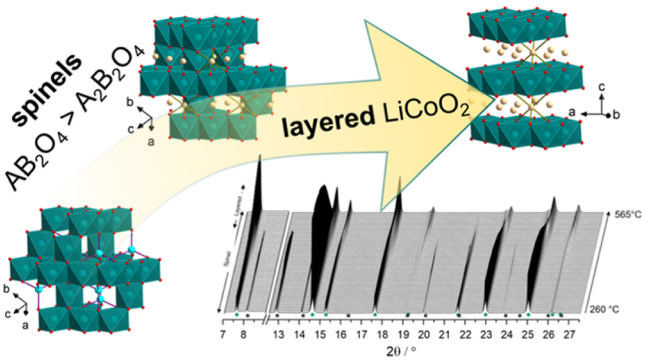

INTRODUCTION

Cobalt oxides and hydroxides are technologically important materials that have been adopted for a variety of applications including positive battery electrode materials[1−4] (Li_xCoO_2 and Na_xCoO_2), thermoelectrics[5,6] ($Na_2Co_2O_4$ and $Ca_3Co_4O_9$), oxidation catalysts[7,8] (Co_3O_4), superconductors[9] and supercapacitors[10−12] [CoOOH and $Co(OH)_2$]. These materials crystallize in structurally related phases containing CoO_6 octahedra, often with close-packed O^{2-} anions, but are otherwise differentiated by the arrangement and stacking of these units and the distribution or ordering of Co and other cations relative to the oxygen sublattice. One of the most prominent applications of these phases has been the use of the layered lithium cobalt oxide $LiCoO_2$ (LCO) as a cathode material for lithium-ion batteries (LIBs). While much attention is devoted to reducing the Co-content in positive electrode materials for electric vehicles, layered LCO remains today the most used cathode material in LIBs for portable electronics applications.[3,4] Even for automotive applications, where low-Co materials are targeted, $LiCoO_2$ is still investigated as a protective coating material. Recent papers have reported on the use of various Co-precursors to coat high Ni-content NCM (lithium Ni−Co−Mn oxide) and $LiNiO_2$ (LNO) cathodes. The precursors are believed to react with residual Li species on the surface of the primary/secondary particles and promote stable long-term cycling.[13−20] In the reported temperature ranges (typically below 700 °C), various ordered or disordered Co-phases may be expected to form, depending on the synthetic conditions and the choice of initial Co- and Li-precursors. These include layered $LiCoO_2$, quasi-spinel $Li_2Co_2O_4$ (also called low-temperature LCO, "LT-LCO", due to the analogous stoichiometry), spinel Co_3O_4, and partially lithiated versions thereof, $Li_yCo_{3-y}O_4$. LCO samples with various structures,[21−26] crystallinities,[27,28] initial Li contents,[29−34] morphologies,[35−38] and/or particle sizes[29,39] have been proven to perform very differently when tested as cathode materials in LIB cells; thus, the same parameters could influence how the Co coating affects the electrochemical performance of the NCM materials. However, understanding the composition and crystallinity of a material used as coating, present in very small amounts, requires a priori insight into its thermodynamic crystallization pathway as a function of temperature and choice of precursors. Moreover, despite the

fact that layered LCO is expected (from the thermodynamics perspective) to be the stable ground-state structure at all temperatures, some thermodynamic and especially kinetic aspects influencing its crystallization are still debated[22,40,41] and are worth further investigation.

To resolve the presence of these phases at various stages of synthesis, specialized techniques, such as variable temperature *in situ* X-ray diffraction (XRD), can be used to study the phase evolution of solid-state reactions in real time.[42−45] Through the advent of improved experimental capabilities, especially using synchrotron sources, these studies can provide profound insights into reaction pathways and differentiate kinetic and thermodynamic aspects of the reaction.[46] *In situ* XRD has been used by various groups to follow the formation of layered LCO from various precursors, such as Co and Li acetates[47] and industrially relevant Co_3O_4 + Li_2CO_3.[22,40,41] The use of the latter is favored by industry to achieve a practical tap density as larger particle sizes (∼15 to 30 μm) are systematically reported in the final LCO powders.[39,48−50] For the same reasons, evidencing the temperature range at which layered LCO forms remains the main focus of most studies, without detailed structural analysis of the low-temperature phases. Several studies in fact adopt a pre-annealing step prior to the *in situ* experiments, which may contribute to the lack of information available on low-temperature phases since a heat treatment, even at moderate temperatures, may change the initial composition and structures of the blend quite drastically.[45] The temperature at which lithiated intermediates first form will also be affected by the choice of Li salts, whose melting points vary considerably (∼286 °C for CH_3COOLi, ∼465 °C for LiOH, and ∼723 °C for Li_2CO_3), thereby changing the temperature ranges in which the lithiation kinetics are enhanced. On the other hand, *in situ* XRD is not without limitations. Intermediate phases can be difficult to resolve in patterns due to their poor crystallinity after nucleation, and products with structural similarity[21,51−53] may be difficult to distinguish from one another. This issue is particularly pertinent for the reaction to form LCO since (as mentioned above) several related structures are known to exist, which share the same oxygen sublattice and exhibit similar lattice constants. A proper identification of phases thus requires the use of additional characterization techniques, among which Raman spectroscopy has been shown to be highly relevant to probe (non)lithiated cobalt phases. Indeed, characteristic Raman fingerprints have been reported for Co-oxides, hydroxides, and oxyhydroxides (see Table 1), making Raman spectroscopy a key technique to distinguish them. Additionally, spectral changes, such as loss of intensity, shifts, and broadening of bands, were found to be correlated to the Li concentration in Li_xCoO_2 electrodes as reported by Inaba *et al.*[54] As a result, Raman spectroscopy and microscopy have gained popularity[55−59] to examine the variations of Li concentration in LCO-based electrodes in a non-destructive manner (*i.e.*, effectively probing the state-of-charge spatial distribution across LCO particles).

Here, we present a detailed analysis of the phase evolution during the formation of LCO from β-$Co(OH)_2$ and Co_3O_4 precursors with LiOH, using a combination of *in situ* variable temperature XRD and *ex situ* Raman spectroscopy. The temperature ranges at which the transitions to spinel, quasi-spinel, or layered lithium cobalt oxide compounds occur are resolved and found to show dependence on the cobalt

Table 1. Expected Structural Parameters and Raman Shifts of Observed Phases, As Reported in the Literature

	XRD			Raman spectroscopy	
phase	space group	cell parameters	ICSD code	total irreducible representation according to factor group analysis R: Raman-active, IR: infrared-active, N: inactive, A: acoustic	Raman shifts (cm^{-1})
β-$Co(OH)_2$	$P\bar{3}m1$ Z = 1	a = 3.18098(4) Å,c = 4.63405(9) Å, V = 40.61 Å^3,α = β = 90°,γ = 120°	257275 ref 66	Γ = $2A_{1g}(R)$ + $3A_{2u}(IR)$ + $2E_g(R)$ + $3E_u(IR)$	250−252 (E_g), 427−431 (A_{1g}), 503−504 (E_g), 3572 − 3577 (A_{1g}) refs 8, 67−69
3R-CoOOH	$R\bar{3}mZ$ = 3	a = 2.851(1) Å,c = 13.150(5) Å, V = 92.57 Å^3,α = β = 90°,γ = 120°	22285 ref 70	Γ = $A_{1g}(R)$ + $3A_{2u}(IR)$ + $3E_u(IR)$ + $E_g(R)$	503−513 (E_g), 590−640 (A_{1g}) refs 8, 6371−75
2H-CoOOH	$P6_3/mmc$ Z = 2	a = 2.855 Å,c = 8.805 Å,V = 62.15 Å^3, α = 90°,β = 90°,γ = 120°	56288 ref 76	Γ = $A_{1g}(R)$ + $3A_{2u}$ + $2B_{1g}(R)$ + $2B_{2u}$ + $2E_u$ + $2E_{2g}(R)$ + $3E_{1u}$ + $E_g(R)$	
Co_3O_4	$Fd\bar{3}mZ$ = 8	a = b = c = 8.0835(6) Å,V = 528.8 Å^3, α = β = γ = 90°	24210 ref 77	Γ = $A_{1g}(R)$ + $E_g(R)$ + $F_{1g}(N)$ + $5F_{1u}(1A+4IR)$ + $3F_{2g}(R)$ + $2A_{2u}(N)$ + $2E_u(N)$ + $2F_{2u}(N)$	175−200 (F_{2g}), 485−495 (E_g), 515−525 (F_{2g}), 610−620 (F_{2g}), 688−710 (A1g) refs 8,65,78−81
$Li_2Co_2O_4$	$Fd\bar{3}mZ$ = 8	a = b = c = 7.994(1) Å,V = 510.85 Å^3, α = β = γ = 90°	74320 ref 21	Γ = $A_{1g}(R)$ + $E_g(R)$ + $F_{1g}(N)$ + $2F_{2g}(R)$ + $3A_{2u}(N)$ + $3E_u(N)$ + $5F_{1u}(IR)$ + $3F_{2u}(N)$	480−486,445−449,585−592,602−608 refs 23−25,82−85
$LiCoO_2$	$R\bar{3}mZ$ = 3	a = 2.8161(5) Å,c = 14.0536(5) Å, V = 96.52 Å^3,α = β = 90°, γ = 120°	51182 ref 86	Γ = $A_{1g}(R)$ + $2A_{2u}(IR)$ + $E_g(R)$+ $2E_u(IR)$	485−492 (E_g), 595−601 (A_{1g}) refs 23−25,54,83−85 and 87

precursor used in the reaction. Further to this, the presence of several intermediate phases is evidenced.

EXPERIMENTAL SECTION

,

Materials. $LiOH{\cdot}H_2O$ (BASF SE) and $Co(OH)_2$ (Sigma-Aldrich) were used as precursors in this study. The Co_3O_4 precursor was prepared by heating of $Co(OH)_2$ to 600 °C for 6 h in air. The precursor blends were prepared with a slight lithium excess, $n(Li)/n(Co)$ = 1.04:1, and they were mixed thoroughly with a mortar and pestle. To prepare samples for *ex situ* measurements, ∼5 mg of the precursor blends were weighted into an alumina crucible and heated to the target temperature under synthetic air flow at a rate of 3 °C min^{-1} and then held for 10 min. The small quantity of powder was chosen to reflect the scale used for the variable temperature *in situ* experiments, as detailed below. Samples were then packed into 0.3 mm borosilicate glass capillaries for analysis (XRD and Raman spectroscopy).

X-ray Diffraction. Variable temperature *in situ* XRD experiments were carried out at the material science and powder diffraction (MSPD) beamline at the ALBA Synchrotron, Cerdanyola del Vallès, Barcelona, Spain.[60] This beamline utilizes a one-dimensional silicon-based position-sensitive MYTHEN detector in Debye−Scherrer geometry, enabling fast data acquisition with excellent statistics and high angular resolution. Data were collected at a wavelength of λ = 0.61887 Å, determined using a NIST Si 640c standard reference material (SRM), in the angular range 0.376° < 2θ < 52.144° ($Q \approx$ 0.0686−8.924 $Å^{-1}$). The instrumental contribution to the peak broadening was obtained by measuring a highly crystalline $Na_2Ca_3Al_2F_{14}/CaF_2$ (NAC) sample as the line broadening reference.

The homogeneously mixed precursors were loaded into an open-ended quartz capillary of diameter 1 mm for the heating experiments. The filled capillary was mounted on a capillary flow cell similar to the one reported by Chupas *et al.*[61] This setup allows placing the capillary in the center of the diffractometer goniometer while also flowing a stream of gas through the capillary. During data collection, the whole setup was "rocked" by rotating around the goniometer center by ±5° to improve powder averaging. The sample was heated using a hot air-blower (FMB Oxford) placed above the capillary. The temperature at the hot-blower tip (where a thermocouple was placed) had been previously calibrated at the beamline using the thermal expansion of the Si powder as the reference. The blends were heated under synthetic air flow at rates of 3 and 20 °C min^{-1} to a dwell temperature of 700 °C, with a pattern collection time of 60 s.

Refinement of structural models against the XRD data was carried out using GSAS-II.[62] The observed structures could be indexed to previously reported materials from the inorganic crystal structure database (ICSD), see Table 1. An uneven background contribution could be attributed to the quartz capillary, which was fitted to the first dataset using a Chebyshev polynomial function with 26 terms and fixed thereafter. For sequential refinements, the scale factors (or phase fraction) of each phase were initialized to zero and allowed to refine only for the patterns where each phase was observed. Unit cell parameters were also allowed to vary in the regions where each phase was observed, including two-phase regions. To account for differences in the crystallinity of phases observed during heating, sample contributions to peak broadening were modeled using isotropic size/strain parameters, which were determined individually for each phase.

Diffraction patterns of *ex situ* samples were collected using a STOE Stadi-P diffractometer with a DECTRIS MYTHEN 1K strip detector in Debye−Scherrer geometry. The instrument uses a Mo anode, which provides a single X-ray wavelength of λ = 0.70926 Å. The instrumental contribution to the peak broadening was obtained by measuring a NIST 640f Si SRM.

Raman Spectroscopy. All Raman spectra were collected in the 100−1500 cm^{-1} range using a Renishaw inVia confocal microscope equipped with a charge-coupled device camera. An Nd:YAG laser was used as the excitation source (λ = 532 nm). All spectra were collected in back-scattering geometry, and the spectral resolution was about 1.25 cm^{-1}. A 20× objective was used to focus the laser light onto the sample surface. $Co(OH)_2$, CoOOH, and even CoO have been shown to easily degrade and turn into Co_3O_4 when subjected to high levels of laser irradiation (P > 0.1 mW).[63−65] Thus, the laser power was fixed to 0.1%, corresponding to an output power of P = 0.06 mW. For each sample, spectra were collected on three different spots to ensure consistency over different regions.

RESULTS

Overview of (Lithiated) Co Oxide and Hydroxide Structures. Various methods can be used to prepare layered LCO, for example, sol−gel or microwave synthesis, while solid-state reactions are generally favored for industrial applications (in particular for use as a cathode material for LIBs). High annealing temperatures (ϑ > 650 °C) are usually required to form layered LCO by heat treatment of cobalt and lithium precursors under an oxidative atmosphere (air and O_2). This helps explain why the latter phase is commonly referred to as "high-temperature" LCO (HT-LCO) in the literature. Other cobalt phases can be formed at lower temperature during the solid-state reaction, whose structure and chemical composition depend on the actual annealing temperature and choice of initial cobalt precursor. This article focuses on the use of β-$Co(OH)_2$ and Co_3O_4 as reactants, with $LiOH{\cdot}H_2O$ as the Li source. Their structures are schematically shown in Figure 1. Brucite β-$Co(OH)_2$ crystallizes in the CdI_2 structure ($P\bar{3}m1$ space group, see Figure 1a) and consists of alternating layers of CoO_6 octahedra. All hydrogen atoms occupy the 2*d* Wyckoff positions of the lattice, that is, the interlayer sites. The oxygen stacking sequence along the *c* axis is ABABAB (A and B referring to given oxygen coordinates, see the caption of Figure 1), corresponding to a "1H" stacking sequence according to the nomenclature developed by Bookin and Drits.[88] The use of either "H" or "R" in such nomenclature denotes the hexagonal or rhombohedral nature of the stacking, while the "1" is linked to the stacking periodicity. Co_3O_4 adopts a regular spinel structure, which is indexed in the $Fd\bar{3}m$ space group. All Co^{2+} are found in tetrahedral 8*a* Wyckoff sites, while the Co^{3+} occupies the octahedral 16*d* Wyckoff sites, thereby forming a characteristic edge-sharing CoO_6 three-dimensional spinel framework. Co_3O_4 can easily be obtained from the calcination of β-$Co(OH)_2$ in the presence of oxygen at ϑ > 400 °C, as reported by several groups[71,89,90] and in this work, with the formation of an intermediate CoOOH phase according to the following equations:

$$Co(OH)_2 + {}^1/_4O_2 \rightarrow CoOOH + {}^1/_2H_2O \quad (1)$$

$$3CoOOH \rightarrow Co_3O_4 + {}^3/_2H_2O + {}^1/_4O_2 \quad (2)$$

As such, both Co_3O_4 and CoOOH may be expected to form during the heat treatment of β-$Co(OH)_2$ and $LiOH{\cdot}H_2O$. CoOOH belongs to the heterogenite mineral family and is known to be prone to polymorphism,[76,91−93] making single-polytype syntheses challenging. While a variety of XRD patterns have been reported for CoOOH, the structures of the two most commonly encountered "3R" and "2H" polytypes are schematically shown in Figure 1b,c, respectively. 3R-CoOOH crystallizes in the trigonal crystal system ($R\bar{3}m$ space group), while 2H-CoOOH crystallizes in the hexagonal system ($P6_3/mmc$ space group). Both polytypes are layered compounds, with structures consisting of alternating CoO_2 layers made of CoO_6 octahedra (Co^{3+} in Wyckoff site 3*a* for 3R, in

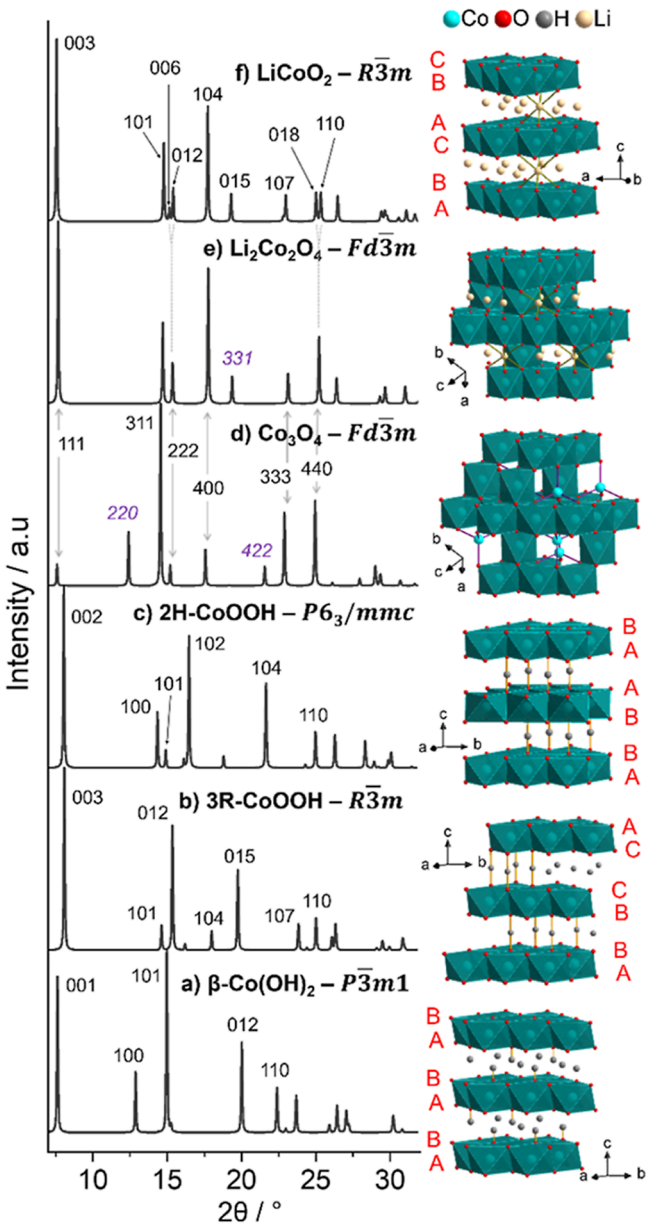

Figure 1. Illustrated crystal structures of cobalt oxides and lithiated cobalt oxides discussed in this study. (right) A, B, and C refer to different oxygen coordinates in the layered structure: A (0, 0, z_A), B (1/3, 2/3, z_B), and C (2/3, 1/3, z_C). (left) Corresponding simulated XRD patterns of the depicted structures at λ = 0.61887 Å.

2*a* for 2H) and H^+ found in the interlayers (3*b* and 2*c* Wyckoff sites, respectively). The main difference between these two polymorphs resides in the periodicity of the oxygen stacking along the *c* axis, with ABBCCA and ABBAAB patterns adopted by 3R- and 2H-CoOOH, respectively.

The layered character of CoOOH phases has been shown to be beneficial in the formation of layered LCO at low temperatures (ϑ = 100 °C) by hydrothermal methods,[94,95] which is one more reason to discard the "high-temperature" (HT) notation usually associated to this phase. However, due to the scarce thermodynamic stability of CoOOH upon heating, solid-state reactions involving the use of CoOOH and a Li salt are expected to form spinel-type materials, such as Co_3O_4, over layered LCO in the low-temperature region. A quasi-spinel $Li_2Co_2O_4$ phase has been reported[21,22,51−53,83,96−101] to form at moderate temperatures (300 °C ≤ ϑ ≤ 600 °C) from such routes, whose structure shares the same CoO_6 octahedra framework as Co_3O_4 (see Figure 1d) This phase is commonly referred to as low-temperature "LT-$LiCoO_2$" in the literature as it shares the same stoichiometry, and its structure is schematically shown in Figure 1e. This phase will be referred to as "$Li_2Co_2O_4$" throughout the rest of the text, while the use of "$LiCoO_2$" will be dedicated to layered LCO ($R\bar{3}m$). In $Li_2Co_2O_4$, the tetrahedral 8*a* sites are unoccupied, unlike spinel Co_3O_4 where the tetrahedral sites are occupied by Co^{2+}. This explains why appellations, such as "pseudo-spinel" or "quasi-spinel", are widely employed in the literature. In $Li_2Co_2O_4$, all cations are found in octahedral sites: Li^+ occupies the 16*c* Wyckoff positions, while Co^{3+} is exclusively found in 16*d* Wyckoff positions. However, various reports[21,52,100,101] have highlighted that $Li_2Co_2O_4$ materials show a certain degree of Li^+/Co^{3+} mixing in the 16*c*/16*d* sites. Finally, normal spinel $LiCo_2O_4$, in which Li^+ are found in the tetrahedral sites, has been prepared from heat treatment of chemically de-intercalated layered $Li_{0.5}CoO_2$ by Choi and Manthiram.[102,103] The same authors showed that they could not synthesize it by a conventional solid-state reaction of Li_2CO_3 and Co_3O_4, thus making $LiCo_2O_4$ an unlikely intermediate. However, spinel intermediates with a cationic distribution among the tetrahedral site ($Li_xCo_{1-x}Co_2O_4$) have been proposed[101,104−107] to temporarily form during the onset of lithiation of Co_3O_4. Similarly to quasi-spinel $Li_2Co_2O_4$, all Li^+ and Co^{3+} ions occupy octahedral sites in layered LCO (see Figure 1f). However, as all CoO_6 and LiO_6 octahedra are found in alternating planes along the *c* axis, a rhombohedral unit cell can be used to describe the layered character ($R\bar{3}m$ space group).

Simulated XRD patterns for all Co-phases mentioned above are shown in Figure 1. Similarities may be observed when comparing these patterns. Layered LCO and quasi-spinel $Li_2Co_2O_4$ have almost identical patterns, with the same O stacking and all Li^+ and Co^{3+} ions found in octahedral coordination. However, with all CoO_6 and LiO_6 octahedra being found in the same alternating (*a*, *b*) planes along the *c* axis in $LiCoO_2$, additional 006 and 009 reflections appear in its XRD pattern, though their intensities remain very weak. A single reflection of quasi-spinel $Li_2Co_2O_4$ is expected at *d* = 1.414 Å (found at ∼ 25.1° in Figures 1 and S1), which can be attributed to the 440 reflection of the structure. For layered LCO, instead, two reflections are expected at similar *d*-spacings of 1.408 Å and 1.425 Å, which originate from the (018) and (110) planes. Because both $Li_2Co_2O_4$ and Co_3O_4 crystallize in the $Fd\bar{3}m$ space group and because of a small difference in their *a* parameter (8.00 Å *vs* 8.08 Å), most of the reflections appear at very similar 2θ positions. The main difference resides in the intensity of the 220 and 331 reflections. The former is one of the most intense lines in the case of Co_3O_4, while its intensity is negligible for $Li_2Co_2O_4$. The opposite trend is observed for the 331 reflection. Although it might be enough to evidence which phase is formed when working with single-phase samples, mixtures of the two, especially when crystallizing in sequence, will be hard to resolve by the use of XRD alone, as illustrated with simulated XRD patterns of mixtures (see Figure S1). When both $Fd\bar{3}m$ phases are detected by XRD, two 440 reflections can be observed in the corresponding pattern, giving the illusion of a doublet that can easily be confused for 018 and 110 normally characteristic of layered LCO. Additionally, large line broadening due to poor crystallinity

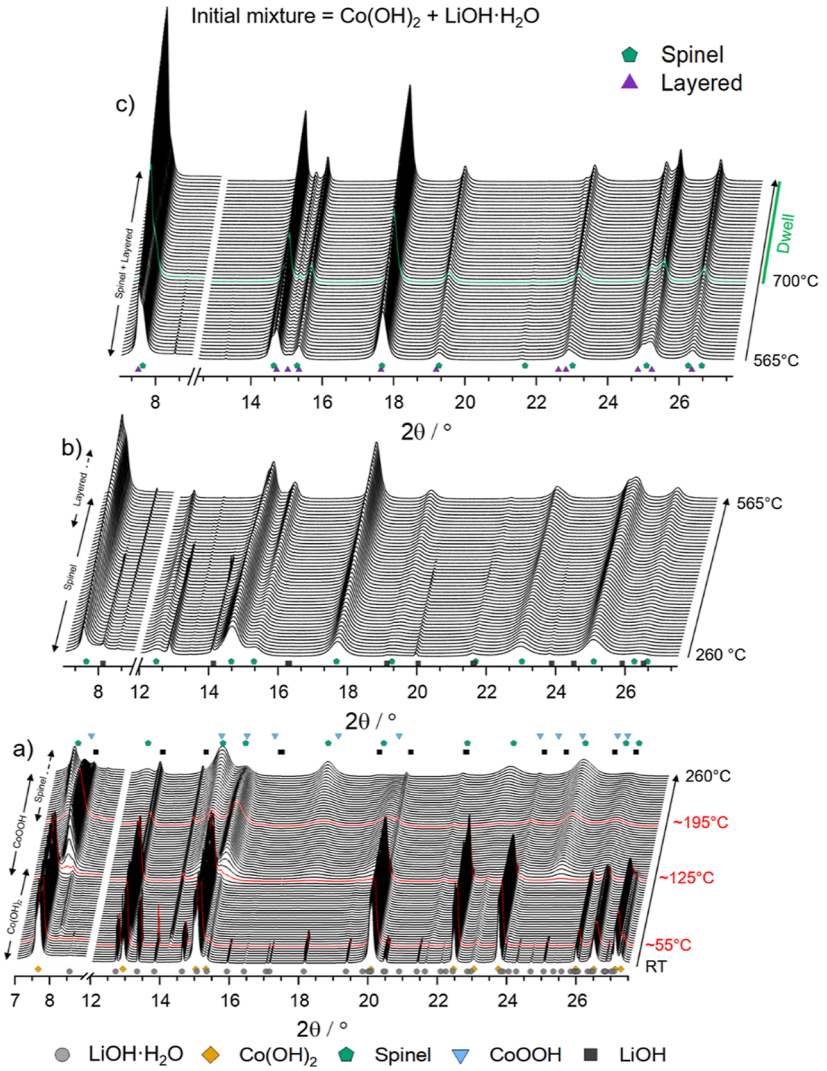

Figure 2. Evolution of diffraction data observed during heating of the $LiOH{\cdot}H_2O/Co(OH)_2$ blend. (a) RT−260 °C, (b) 260−565 °C, and (c) 565−700 °C (with 1 h dwell). Wavelength: λ = 0.61887 Å.

of samples prepared at moderate temperatures may make the interpretation of XRD even more challenging.

In the following, Raman spectroscopy will be coupled to synchrotron XRD to properly evidence the phases formed during the reaction of our two blends, namely, $Co(OH)_2$ + $LiOH{\cdot}H_2O$ and Co_3O_4 + $LiOH{\cdot}H_2O$.

Reaction of $Co(OH)_2$ with $LiOH{\cdot}H_2O$. Figure 2 shows the evolution of diffraction data collected during the heating of the $Co(OH)_2/LiOH{\cdot}H_2O$ blend (1:1.04 molar ratio) to 700 °C at a heating rate of 3 °C min^{-1}. Contour plots can be found in Figure S2a. Note that data were also collected with a heating rate of 20 °C min^{-1} (see Figure S3a). All phases formed during the heating at 3 °C min^{-1} rate were evidenced in similar temperature ranges in the data collected at 20 °C min^{-1}. For more clarity, the XRD patterns have been divided to highlight three temperature ranges: (a) low-temperature domain, from RT to 260 °C, (b) mid-temperature domain, from 260 to 565 °C, and (c) high-temperature domain, from 565 to 700 °C, including 1 h of dwell at 700 °C. Multiphase sequential Rietveld refinement was used to model the structural evolution of the observed phases, and further details are provided in the Experimental Section. The refined cell volumes and phase fractions are shown in Figure 3. Examples of the quality of fit to the selected patterns are shown in Figure S4.

In the low-temperature domain (Figure 2a), the dehydration of $LiOH{\cdot}H_2O$ can be observed first at $\vartheta \approx 55$ °C. The initial cell volume of β-$Co(OH)_2$ is found to be 40.827(1) $Å^3$, and it increases linearly up to a temperature of 125 °C, where the volume is 41.147(3) $Å^3$, in good agreement with the literature.[8,75,108,109] At ϑ = 125 °C, new reflections appear at $2\theta \approx 8.0$, 15.3, and 19.7°, which can be ascribed to the CoOOH structure. These reflections are significantly broadened compared to those of the initial β-$Co(OH)_2$, most likely due to smaller coherent scattering domains in the former phase. All diffraction lines of CoOOH can be indexed using the $R\bar{3}m$ space group, suggesting that this formed cobalt oxyhydroxide adopts the 3R-stacking, as depicted in Figure 1b. Apart from that, no broad reflection is observed in the 21−23° range (see simulated pattern in Figure 1), which would be more characteristic of the 2H-polytype. CoOOH first briefly coexists with β-$Co(OH)_2$ from 125 to 150 °C and then exists as a single phase until 195 °C (see Figure 3b). The cell volume of CoOOH also increases with temperature (see Figure 3a), from an initial value of 94.03(2) to 94.36(3) $Å^3$ at 235 °C. At ϑ = 195 °C, the growth of new broad reflections is observed,

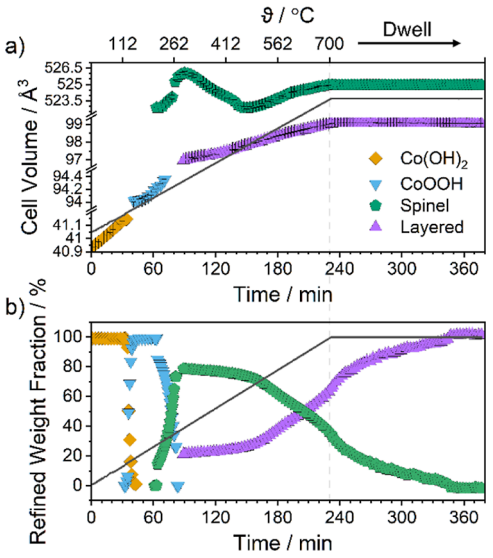

Figure 3. (a) Unit cell volumes and (b) weight fractions determined from refinement of structural models against the XRD data collected during heating of the $LiOH{\cdot}H_2O/Co(OH)_2$ blend. The solid line reports the temperature evolution, referring to the top *x* axis.

which can be indexed to the $Fd\bar{3}m$ space group. A structure with this space group could be expected for spinel Co_3O_4 and quasi-spinel $Li_2Co_2O_4$, which both would exhibit very similar XRD patterns as previously discussed. In any case, distinguishing both spinels is not possible here due to the significant line broadening observed in XRD patterns collected during the annealing of this blend. Refinement of the *in situ* XRD data was thus performed using a single cubic phase. This phase will be referred to as "spinel" for the discussion hereafter. The formation of Co_3O_4 by annealing from CoOOH has been reported inconsistently in the literature to occur at temperatures ranging from 125 to 200 °C.[90,94,95] As a result, the spinel phase detected here presumably consists of Co_3O_4, at least when it is first formed at 195 °C. This is supported by the fact that LiOH is still largely observed as a crystalline phase at this temperature. The CoOOH and spinel continue to coexist until the temperature reaches 270 °C. The cell volume of the spinel phase is observed to increase to a maximum value of 526.05(15) Å^3 at ϑ = 265 °C, as would be expected due to thermal expansion. However, beyond 290 °C, the cell volume begins to decrease considerably to a value of 522.86(9) Å^3 at 455 °C. This behavior could be attributed to the lithiation of the material, occurring concurrently to its oxidation. While the large lithium ions enter the structure and could increase the overall cell volume, Co oxidation results in a strong ionic size reduction, so that overall the unit-cell volume decreases. A similar behavior has also been observed[45,110,111] during the lithiation of other layered oxide materials, such as cubic $Li_yNi_{1-y}O$. Both smaller *a* parameter and cell volume are also expected in the case of lithiated cobalt spinels (*e.g.* $Li_2Co_2O_4$, *a* = 7.8−8.0 Å) compared to Co_3O_4 (*a* = 8.08−8.10 Å) (see Table 1). This decrease in cell volume coincides with the reduction in intensity of the LiOH reflections and a gradual increase in intensity of the 111, 222, and 400 reflections of the spinel phase, at 7.7, 15.4, and 17.8°. The reflections of the spinel phase continue to persist until the end of the mid-temperature domain, as shown in Figure 2b. Toward the end of this region, beginning at $\vartheta \approx$ 535 °C, a sharp shoulder on the left of the 111 spinel reflection is observed to grow, which corresponds to the 003 reflection of the layered structure. Simultaneously, a weak reflection appears at ∼15° and would also be expected as the 006 reflection of the layered structure as well as the splitting of the 440 spinel reflection at ∼25° into the 018 and 110 reflections of the layered phase. Reflections from both of these phases become sharper with (i) the increase of temperature and (ii) time during the dwell at 700 °C, due to growth of larger coherent domains (see Figure 2c). The spinel and layered phases coexist up to 700 °C and further during the dwell. The fraction of the spinel phase becomes <5% approximately 90 min after the dwell at 700 °C started. The formation of layered LCO by solid-state reactions at temperatures below 500 °C has been suggested in some publications, and the refined weight fractions generated from the data collected in this study also suggest a non-negligible presence of layered LCO already at such low temperatures. Based on XRD alone, the broad reflections of the spinel phase, coupled with the similar reflection positions expected for layered LCO, make it however difficult to precisely deconvolute the two phases. This may result in the incorrect attribution of some diffraction intensity to the layered phase at low temperatures by the Refinement software. Hence, the refined weight fractions cannot be considered entirely reliable on their own.

To clear any misconceptions that could arise from interpreting the *in situ* XRD alone, *ex situ* samples were prepared from a blend of $LiOH{\cdot}H_2O$ and $Co(OH)_2$ at targeted temperatures and further analyzed by both XRD and Raman spectroscopy. As stated earlier, $Co(OH)_2$, CoOOH, Co_3O_4, lithiated Co-spinels (*e.g.*, $Li_2Co_2O_4$), and layered LCO each have very specific Raman fingerprints (see Table 1). Thus, one of the main advantages is the possibility to further resolve the spinel domain evidenced by *in situ* XRD and, in particular, to provide evidence of the formation of the quasi-spinel $Li_2Co_2O_4$. The XRD patterns of all *ex situ* samples can be found in Figure S5a. For each targeted temperature, we successfully formed the phases expected from *in situ* XRD: (i) CoOOH at ϑ = 125 °C, (ii) spinel(s) at ϑ = 300−525 °C, and (iii) layered LCO (first observed at ϑ = 610 °C). Figure 4 shows the 170−760 cm^{-1} region of the Raman spectra collected from the same series of *ex situ* samples.

Two of the three expected low-frequency (<800 cm^{-1}) bands of brucite-type β-$Co(OH)_2$[68] can clearly be observed at 431 cm^{-1} (A_{1g}) and 503 cm^{-1} (E_g) in the Raman spectrum of the initial $Co(OH)_2/LiOH{\cdot}H_2O$ blend. The third low-frequency band expected at around 253 cm^{-1} is too broad to be observed here. These values are well within the respective 251−253, 427−431, and 503−504 cm^{-1} ranges previously reported in the literature for these modes.[8,69,109] After heating the blend to 125 °C, the aforementioned Raman bands are no longer visible and three new Raman bands appear at 505, 597, and 640 cm^{-1} in a much broader envelope ranging from 400 to 650 cm^{-1}. This fingerprint is characteristic of CoOOH, as reported by Pauporté *et al.*[63] and other groups[72,73,75,109,112]. The detection of the CoOOH phase in this temperature range is in line with the *in situ* XRD data presented earlier. The broadness of the Raman signal may be explained by (i) CoOOH having very small coherent domains, as also revealed by the broad Bragg reflections in the corresponding XRD patterns, (ii) its structure being far from ideal, most likely containing defects, such as stacking faults, and/or (iii) the possibility of small domains adopting another stacking-type, such as 2H instead of 3R, due to the known polymorphism in

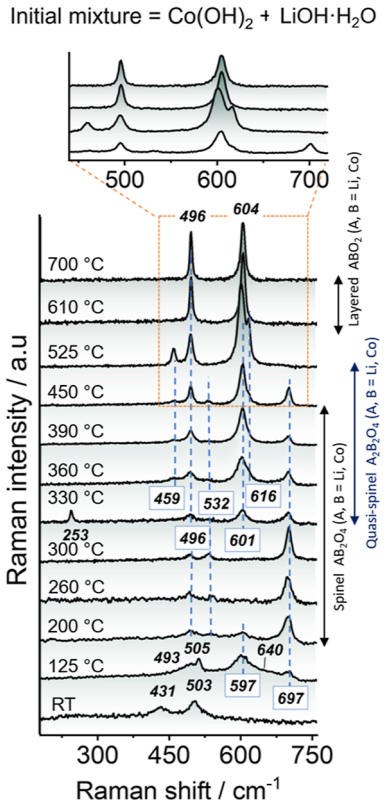

Figure 4. Raman spectra collected *ex situ* from samples prepared by heating the $LiOH{\cdot}H_2O/Co(OH)_2$ blend to selected temperatures.

CoOOH (which would be hard to detect by XRD due to the low crystallinity). While the bands corresponding to CoOOH dominate the spectrum of the sample prepared at ϑ = 125 °C, two new additional bands can be distinguished at 493 and 697 cm^{-1}. At 200 °C, the reported Raman spectrum consists of these two new bands plus three additional modes located at 196, 532, and 616 cm^{-1}. The bands expected at 196 and 616 cm^{-1} have extremely weak intensities and are virtually absent in the survey spectrum, which is a consequence of significant bands broadening and poor signal-to-noise ratio. Note that these two bands are always the less intense of the five when recording Raman data of Co_3O_4 at λ = 532 nm.[65,81,113] This five-mode fingerprint is characteristic of normal spinel Co_3O_4, whose bands have been assigned to the $F_{2g}(1)$, $F_{2g}(2)$, E_g, $F_{2g}(3)$, and A_{1g} vibrational modes (from lowest to highest frequency).[8,63,65,79,80] Thus, this suggests the presence of some Co_3O_4 already at ϑ = 125 °C by Raman spectroscopy despite the lack of Bragg reflections in the *in situ* or *ex situ* XRD patterns. The content of Co_3O_4, coupled with scattering domains that may be either too small or not crystalline enough, may prevent it from being detected by XRD. It is also possible that Co_3O_4 could form under the conditions used to prepare the *ex situ* samples. In any case, this is in line with the literature, where a Co_3O_4 impurity is frequently observed[94,95] in CoOOH samples synthesized between 125 and 130 °C. The same Co_3O_4 bands are the predominant signals for the samples prepared up to 300 °C, confirming that these are composed of single-phase Co_3O_4. All spectra of samples prepared between 330 and 450 °C, that is, within the temperature range of the spinel domain highlighted in Figures 2 and 3 (*in situ* XRD results), exhibit instead the same six bands located at 459, 496, 532, 601, 616, and 697 cm^{-1}. The Raman spectrum of the sample prepared at ϑ = 330 °C differs slightly from all other Raman spectra in this spinel domain temperature range, with no clear band observed at 616 cm^{-1} and an unexpected low-frequency band at 253 cm^{-1}. This feature will be discussed in more detail below in the text. Of the six Raman bands observed in the spinel spectra, four (located at 459, 496, 601, and 616 cm^{-1}) can be assigned to the characteristic $F_{2g}(1)$, E_g, A_{1g}, and $F_{2g}(2)$ modes[23,24,82−85,114] expected for quasi-spinel $Li_2Co_2O_4$, thereby confirming that its formation starts in the temperature range 300−330 °C. This result is in line with the decrease of the cell volume observed upon heating, suggesting that the lithiation of the spinel phase begins in this specific temperature range. The frequencies reported here for quasi-spinel $Li_2Co_2O_4$ are slightly higher than values available in the literature and may be caused by local disorder or far-from-ideal Li, Co stoichiometries. The other two bands, located at 532 and 697 cm^{-1} and already observed at lower temperatures, indicate that some Co_3O_4 still remains. Note that the other two E_g and $F_{2g}(3)$ modes of Co_3O_4 were previously observed at the same 496 and 616 cm^{-1} frequencies and may still be present here (overlapping with the E_g and $F_{2g}(2)$ modes of $Li_2Co_2O_4$). The full width at half-maximum (FWHM) of all these bands decreases as the annealing temperature increases, most likely due to growth of larger coherent domains, consistent with a similar decrease of line broadening in the *in situ* XRD patterns collected in the same temperature range. A higher degree of Co/Li cation ordering in the 16*c* and 16*d* sites of $Li_2Co_2O_4$ for samples prepared at the upper end of the 300−450 °C temperature range may also contribute to the decrease in FWHM.[21,52,100,101] At ϑ = 525 °C, the only bands observed are those of pseudo-spinel $Li_2Co_2O_4$, suggesting complete conversion from Co_3O_4, in good agreement with the phase evolution from *in situ* XRD. However, some layered LCO, whose bands would overlap with the 496 and 600 cm^{-1} modes of $Li_2Co_2O_4$, might already be present in the sample as the relative intensity of all four modes slightly deviates from the expected ratio reported for a λ = 532 nm laser.[82,115] Upon increasing the annealing temperature to 610 °C and beyond, the migration of Co^{3+} and Li^+ into their respective 3*a* and 3*b* Wyckoff sites is complete, yielding layered LCO, whose expected A_{1g} and E_g (gerade) modes are located at 496 and 604 cm^{-1}. These values are slightly higher than those reported by other groups, although Kushida and Kuriyama[116] observed similar frequencies for layered LCO. Again, local disorder caused by cation mixing or variations from the ideal Li/Co = 1.0 stoichiometry may cause the frequency shift, although Raman bands of Li-deficient LCO are usually shifted toward lower frequencies.[54,117] While some of the reflections from $Li_2Co_2O_4$ were still observed by *in situ* XRD at ϑ = 700 °C, no characteristic band of this phase is found in the corresponding Raman spectrum.

As mentioned earlier, an unexpected band located at 253 cm^{-1} appears in the spectrum of the sample prepared at ϑ = 330 °C. This band has never been reported in the literature for Co-based compounds (quasi-spinel or layered). Although a clear assignment of this band is out of scope of this article, several hypotheses are to be considered, suggesting that this band arises from a certain degree of cation disorder. The observation of more bands than expected from factor group analysis in Raman spectroscopy has often been linked to local distortions, inducing local breaks of symmetries and/or the randomization of cationic distribution within the AB_2O_4 spinel-like structures.[118,119] Additionally, the natural cooling

conditions adopted in the preparation of the *ex situ* samples could stabilize samples with a far-from-ideal cation distribution and/or local defects. Julien *et al.* found that in Li(Co, Ni)VO_4 spinels, where Li and (Co and Ni) occupy the 16*c* and 16*d* Wyckoff sites, respectively, analogous to quasi-spinel $Li_2Co_2O_4$, a heterogeneous distribution of Li and (Co and Ni) over these two sites yields additional Raman bands.[120] The possibility of a non-ideal octahedral distribution of Li and Co in $Li_2Co_2O_4$ has been discussed by several authors. Shao-Horn *et al.*[100] provided direct evidence by electron microscopy for LT-LCO samples prepared through solid-state reaction. Julien and Massot also reported[121] an unexpected band at 303 cm^{-1} in the Raman spectrum of spinel $LiMn_2O_4$, which was tentatively explained as being an IR-active mode becoming Raman-active as a consequence of both (i) the Jahn–Teller (JT) distortion of $Mn^{4+}O_6$ octahedra and (ii) the difference in ionic radii of Mn^{3+}/Mn^{4+} distributed among the octahedral sites. While no JT effect is to be expected in Li^+O_6 or $Co^{3+}O_6$ octahedra, the difference of ionic radius between Li^+ and Co^{3+} (0.76 *vs* 0.545 Å) may still be enough to induce a similar breakdown of the IR/Raman selection rules. As a matter of fact, an IR-active band has been reported at ~267 cm^{-1} for pseudo-spinel $Li_2Co_2O_4$ by Huang and Frech[24] and at ~260 cm^{-1} by Julien.[25] Another explanation may involve the formation of a partially or fully lithiated cobalt spinel phase in which the 8*a* tetrahedral site is occupied either by Li^+ or Co^{2+}/Co^{3+}. While most bands have clearly been assigned to their corresponding active modes in the literature,[122] there is still debate regarding the atomic motion involved. However, literature seems to agree that low-frequency bands found at <400 cm^{-1} are linked to the complete translation of tetrahedral AO_4 units within the spinel structure.[78,123–125] Thus, the band at 253 cm^{-1} may be observed due to some remaining Co and/or Li occupying the tetrahedral sites, with a $[Li_xCo_{1-x}]_{8a}[Co_2]_{16d}O_4$ intermediate being formed at $\vartheta \approx 330$ °C. Again, several authors[101,104–107] have speculated that the lithium first diffuses through tetrahedral sites in Co_3O_4. Appandairajan *et al.*[104] showed that solid solutions of $Li_xCo_{1-x}Co_2O_4$ could be formed up to $x = 0.4$. If one considers that the additional band at 253 cm^{-1} does exist because of the formation of $[Li_xCo_{1-x}]_{8a}[Co_2]_{16d}O_4$ upon the first signs of lithiation, this may explain why the band is no longer observed once the solubility limit has been exceeded.

Figure 5 shows the presence of the different phases observed by XRD and Raman spectroscopy as a function of temperature for the $Co(OH)_2$/LiOH·H_2O blend. The combined used of both techniques helped evidencing which structures tend to be stable at a given temperature. $Co(OH)_2$ remains the main Co-phase from RT to 125 °C. CoOOH starts form at this temperature and briefly coexists with $Co(OH)_2$ between 125 and 150 °C. From 150 to 195 °C, CoOOH is found to be the main Co-phase, but it quickly transforms into an AB_2O_4-type spinel phase, most likely consisting of Co_3O_4 at $\vartheta = 195$ °C. A biphasic (CoOOH + AB_2O_4 spinel) domain was detected by XRD from 195 to 270 °C though no CoOOH was detected at $\vartheta = 260$ °C by Raman spectroscopy. According to the *in situ* XRD results, the spinel phase remains until the end of the heat treatment. The Raman spectroscopy results also suggest that AB_2O_4 spinels (Co_3O_4 becoming partially lithiated) might be stabilized as the main polymorph up to a maximum of $\vartheta = 330$ °C in equilibrium conditions (*ex situ*). The formation and stabilization of $A_2B_2O_4$-type spinels ($Li_2Co_2O_4$-like) under the same conditions occurs between 300 and 330 °C, still coexisting with AB_2O_4 spinels up to 450–500 °C. Quasi-spinel $Li_2Co_2O_4$ was found to exist as a single-phase material at 525 °C by Raman spectroscopy though its exact Li, Co stoichiometry remains uncertain. Layered LCO appears at $\vartheta \approx$ 535 °C and is the main phase above 600 °C.

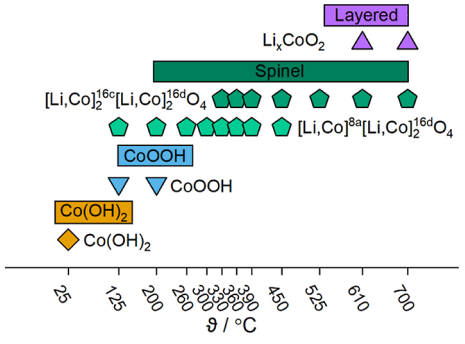

Figure 5. Schematic comparing the phases observed using *in situ* XRD (rectangles) and *ex situ* Raman spectroscopy (symbols) during heating of the LiOH·H_2O/$Co(OH)_2$ blend.

Reaction of Co_3O_4 with LiOH·H_2O. The evolution of diffraction data collected during heating of the Co_3O_4/LiOH·H_2O blend at a rate of 3 °C min^{-1} is shown in Figure 6. Contour plots can be found in Figure S2b. Data collected with a heating ramp of 20 °C min^{-1} are shown in Figure S3b. Similar to Figure 2, the XRD patterns are divided into three temperature domains: (a) from RT to 260, (b) 260 to 565, and (c) 565 to 700 °C including 1 h of dwell at 700 °C. Rietveld refinement was again used to model the structural evolution of the observed phases as the mixture was heated, and the refined cell volumes and phase fractions can be found in Figure 7a,b, respectively, with exemplary refinement profiles shown in Figure S6. Notably, all phases formed exhibit much narrower diffraction lines over the whole temperature range as compared to the $Co(OH)_2$ precursor, indicating larger coherent domains and allowing distinct spinel structures (Co_3O_4*vs* $Li_2Co_2O_4$) to be refined against the data. Both the reduced number of phase transitions and a better crystallinity of the initial Co_3O_4 over $Co(OH)_2$ may be responsible for the overall good crystallinity of phases formed upon annealing. The average domain size from Rietveld refinement was found to be 0.1755(15) and 0.0630(4) μm for Co_3O_4 and $Co(OH)_2$, respectively. As Co_3O_4 was found to be an intermediate phase formed during the solid-state reaction of $Co(OH)_2$ with LiOH·H_2O discussed above, it is not surprising that similar observations arise from the reaction of Co_3O_4 with LiOH·H_2O. After the quick dehydration of LiOH·H_2O until $\vartheta = 260$ °C, the same reflections belonging to the spinel phase (the initial Co_3O_4 precursor) are observed in all XRD patterns. Reflections that can be indexed to a spinel phase also remain in the patterns collected up to ~550 °C. Their positions gradually shift to lower angles as the mixture reaches $\vartheta = 375$ °C, corresponding to an increase in cell volume due to thermal expansion, as shown in Figure 7a. No lithiation of the spinel occurs in this temperature range, which suggests that Co_3O_4 remains the main crystalline phase until 375 °C. The onset of lithiation at 375 °C is indicated by a reduction in cell volume of the spinel phase, until the temperature reaches ~474 °C, during which it decreases from 531.01(2) to 527.67(9) $Å^3$. However, between 435 and 525 °C, a second set of diffraction lines, also indexed in the $Fd\bar{3}m$ space group, is observed to increase in intensity

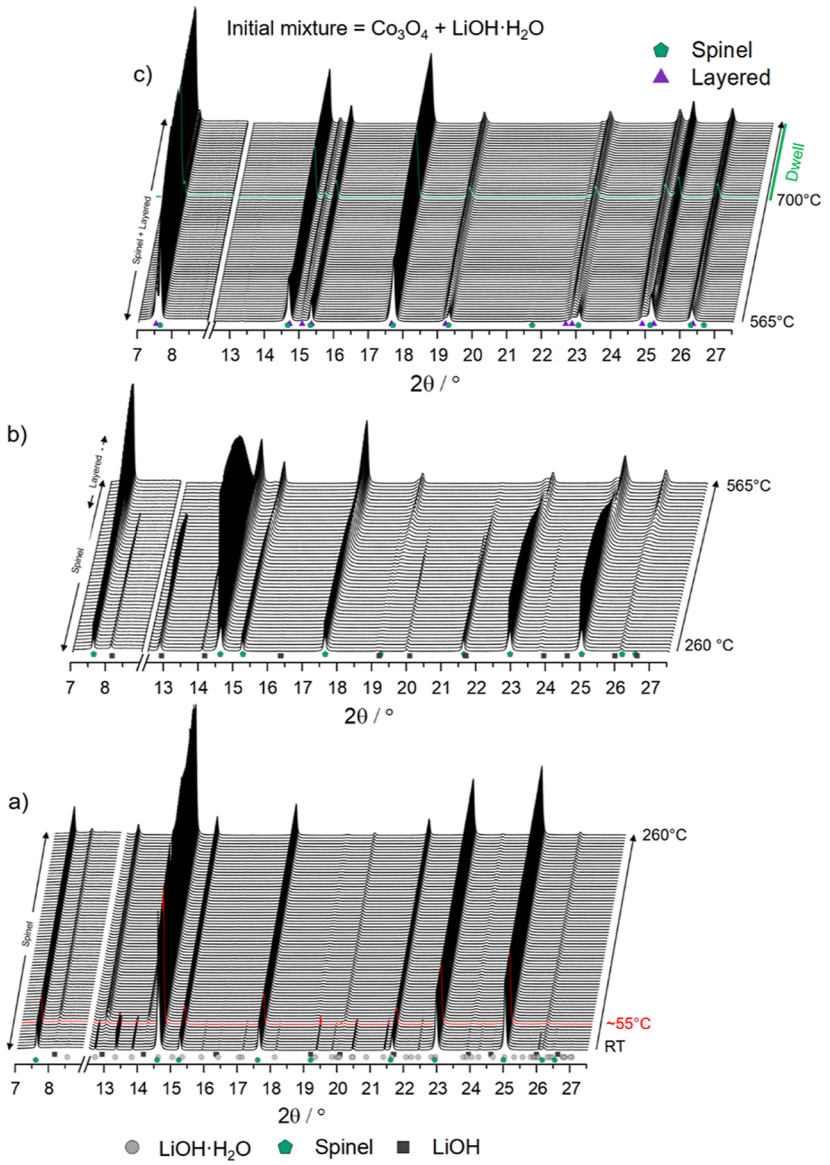

Figure 6. Evolution of diffraction data observed during heating of the $LiOH·H_2O/Co_3O_4$ blend. (a) RT−260, (b) 260−565, and (c) 565−700 °C (with 1 h dwell). Wavelength: λ = 0.61887 Å.

until the temperature of the sample reaches ϑ = 550 °C, revealing the brief coexistence of two spinel phases with different compositions (Li concentrations, highlighted in Figure S6c). The second spinel structure exhibits an initial cell volume of 520.72(2) $Å^3$ at ϑ = 474 °C, reducing to a minimum of 518.06(1) $Å^3$ as the sample reaches ∼550 °C. The melting of LiOH at 465 °C seems to greatly improve the kinetics of the spinel(s) lithiation, as evidenced by the clear change in intensity of the reflections. The intensity of the 111, 400, and 440 reflections at 7.7, 17.8, and 26.5° increases, while a drastic drop in intensity of the 311, 333, and 511 reflections at 14.7, 23.2, and 25.3° is attributed to the fast final lithiation of the spinel(s). The reflections continue to persist until the end of the mid-temperature domain. At ϑ = 540 °C, a sharp shoulder is observed on the left of the 111 spinel reflection, indicating the presence of layered LCO. The gradual emergence of the 006 reflection of the layered phase is also seen at ∼15°, accompanied by the appearance of the 018 and 110 reflections in the same region as the 440 spinel reflection at ∼25°. Both the spinel and layered phases coexist up to 700 °C and further during the dwell. The fraction of the spinel phase becomes <5% approximately 90 min after the dwell at 700 °C started, similar to the $Co(OH)_2$-based blend discussed earlier.

Ex situ samples were also prepared by calcination of a $Co_3O_4/LiOH·H_2O$ blend at targeted temperatures and further analyzed by XRD and Raman spectroscopy. The XRD patterns of the *ex situ* samples can be found in Figure S5b. In line with the *in situ* XRD data, reflections can be indexed to only spinel structures in samples prepared up to 525 °C. Reflections from the layered phase are present at 610 and 700 °C. Raman spectra were collected from the same series of *ex situ* samples and are shown in Figure 8. As expected, because of the overall better crystallinity of the Co_3O_4 precursor compared to $Co(OH)_2$, all Raman bands are very narrow. The characteristic Raman modes of Co_3O_4, located at 205 cm^{-1} ($F_{2g}(1)$), 492 cm^{-1} (E_g), 532 cm^{-1} ($F_{2g}(2)$), 629 cm^{-1} ($F_{2g}(3)$), and 701 cm^{-1} (A_{1g}), are observed in the spectra of (i) the initial blend and (ii) samples annealed at ϑ = 125, 200, 260, 300, 330, 360, 390, and 450 °C. Some of these frequencies seem rather high

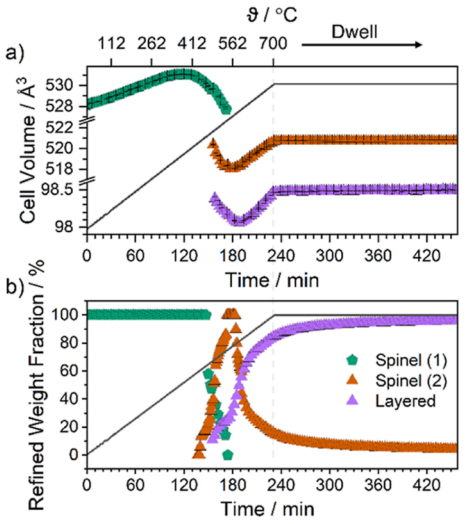

Figure 7. (a) Unit cell volumes and (b) weight fractions determined from refinement of structural models against the XRD data collected during heating of the $LiOH{\cdot}H_2O/Co_3O_4$ blend. The solid line reports the temperature evolution, referring to the top *x* axis.

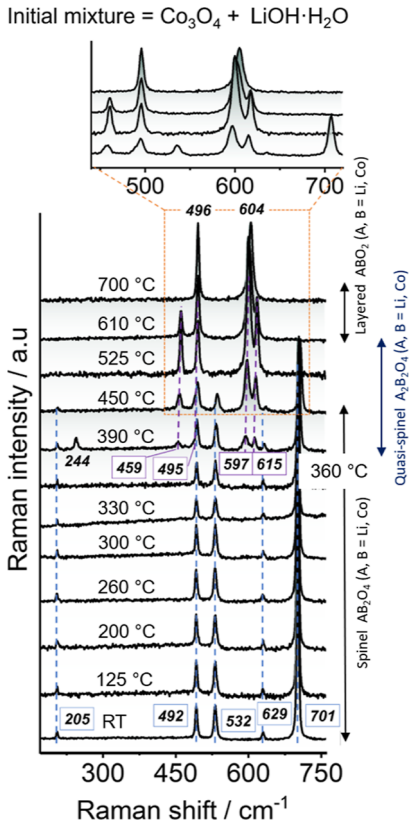

Figure 8. Raman spectra collected *ex situ* from samples prepared by heating the $LiOH{\cdot}H_2O/Co_3O_4$ blend to selected temperatures.

compared to other reports (see Table 1; 205 *vs* 196, 629 *vs* 615, and 701 *vs* 690 cm^{-1}) and may be caused by either local constraints or partial lithiation of Co_3O_4. No other bands exist in the Raman spectra of samples prepared at $125 \leq \vartheta \leq 360$ °C, confirming that the lithiation of the spinel does not occur in such a temperature range, as expected from the increase, rather than decrease, of the unit cell volume, shown in Figure 7a. The four characteristic $F_{2g}(1)$, E_g, A_{1g}, and $F_{2g}(2)$ modes of quasi-spinel $Li_2Co_2O_4$ are first detected for the sample prepared at 390 °C. They are located at 459, 495, 597, and 615 cm^{-1}. This is in good agreement with the *in situ* XRD results, where the first signs of lithiation were seen at 375 °C. A new band is observed at low frequencies (~244 cm^{-1}) when the lithiation of the Co-precursor starts. The unexpected band was found at 253 cm^{-1} in the Raman spectrum of the $Co(OH)_2/LiOH{\cdot}H_2O$ blend annealed at 330 °C, coinciding with the first signs of lithiation. The Raman spectrum for ϑ = 450 °C further confirms that the spinel phase detected by XRD is a mixture of Co_3O_4 and quasi-spinel $Li_2Co_2O_4$ in equilibrium conditions. Quasi-spinel $Li_2Co_2O_4$ is the only existing phase at ϑ = 525 °C with only four modes observed at the same 459, 495, 597, and 615 cm^{-1}. The intensity ratio between all bands[82,115] also confirms that $Li_2Co_2O_4$ exists as a single phase at 525 °C. However, the frequencies for these four bands seem higher than those usually reported, which may again be a result of local disorder or Li, Co stoichiometry variations. As suggested by the change in relative intensities of the 459, 495, 597, and 615 cm^{-1} modes, with both the bands at 495 and 597 cm^{-1} growing at the expense of the other two, a mixture of $Li_2Co_2O_4$ and layered $LiCoO_2$ coexist at 610 °C. At ϑ = 700 °C, layered LCO is the only detected phase, as confirmed by the sole presence of its two characteristic Raman modes centered at 496 cm^{-1} (E_g) and 604 cm^{-1} (A_{1g}). These values are again slightly higher than expected and may indicate local disorder and/or imperfect Li, Co stoichiometries.

The schematic shown in Figure 9 summarizes the phase evolution determined from *in situ* XRD and Raman spectroscopy. A reduced number of phases is found to form over the whole temperature range, logically expected with the direct use of Co_3O_4 as Co-precursor. Distinct spinel structures were detected by *in situ* XRD, between 25 and 475 and 435 and 700 °C. Their Raman spectra suggest that AB_2O_4 and $A_2B_2O_4$-type spinels are again stabilized, similar to what was observed upon annealing of the $Co(OH)_2$-based blend. The formation of the $A_2B_2O_4$ quasi-spinel was first detected at ϑ = 390 °C by Raman spectroscopy. Both AB_2O_4 and $A_2B_2O_4$ spinels coexist between 390 and 450 °C in samples prepared at equilibrium conditions. Quasi-spinel $Li_2Co_2O_4$ was found to exist as a single phase at 525 °C by Raman spectroscopy and to coexist with layered LCO at 610 °C, though their exact Li, Co stoichiometries remain uncertain. Layered LCO appears at around 540 °C and is the main phase at ϑ = 700 °C.

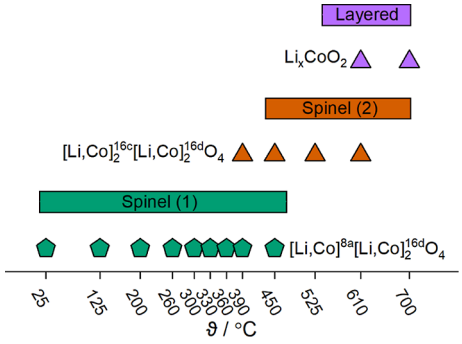

Figure 9. Schematic comparing the phases observed using *in situ* XRD and *ex situ* Raman spectroscopy during heating of the $LiOH{\cdot}H_2O/Co_3O_4$ blend. Rectangles represent data from *in situ* XRD, while symbols represent those obtained by Raman spectroscopy.

DISCUSSION AND CONCLUSIONS

The use of $Co(OH)_2$ as a Co precursor to form LCO by solid-state reaction yields an additional phase at low temperatures (CoOOH) as compared to Co_3O_4. However, after the temperature is passed at which CoOOH transforms into a spinel phase, both $Co(OH)_2$- and Co_3O_4-based systems show great similarities in terms of number of phases formed and temperature ranges of existence, even when changing the heating rate to 20 °C min^{-1}. In both cases, Co-based spinel(s) exist from 270 °C on. Although the exact Li, Co stoichiometries of the cubic phases remain challenging to determine, it is clear that both AB_2O_4 spinels and $A_2B_2O_4$ quasi-spinels (A, B = Li, Co) are formed upon annealing of the blends. Raman spectroscopy results suggest that AB_2O_4 spinels, such as Co_3O_4, or lithiated forms thereof, are the main polymorphs obtained under *ex situ* conditions (in equilibrium conditions) for heat treatments with maximum temperatures of 330 °C (using $Co(OH)_2$) or 390 °C (with Co_3O_4). Forming quasi-spinels of formula $A_2B_2O_4$ (analogous to $Li_2Co_2O_4$) thus requires annealing the initial blends at higher temperatures. Note that even from ~360−390 to 450 °C, quasi-spinels $A_2B_2O_4$ and spinels AB_2O_4 were still found to coexist in *ex situ* samples, with the relative proportions changing as a function of temperature. The higher the annealing temperature, the more $A_2B_2O_4$ is formed at the expense of AB_2O_4. Irrespective of the choice of the initial Co-precursor, $A_2B_2O_4$ was only obtained in single phase form at ϑ = 525 °C *ex situ*, with subsequent formation of layered LCO at ϑ = 535−540 °C. Note that a small fraction of the cubic phase was still detected at the end of our *in situ* XRD experiments, but not by Raman spectroscopy in the *ex situ* samples. The side reaction of Li with the quartz capillary may be responsible for this.

Several authors[101,104−107] have proposed that lithiation of Co_3O_4 first involves Li diffusion into tetrahedral (8*a*, 8*b*) sites (forming $Li_xCo_{3-x}O_4$), accompanied by the redistribution of Co into octahedral sites (16*c* and 16*d*), followed by Li migration also to octahedral sites (16*c*). The full Co oxidation and migration to octahedral sites, as well as concurrent introduction of Li into octahedral sites, may easily yield intermediate products with spinel structure and containing both tetrahedral Co and octahedral Li as metastable compositions $[Co^{II}_{2(1-y)/(2+y)}]_{8a}[Li_{6y/(2+y)}]_{16c}[Co^{III}_2]_{16d}O_4$ (with y from 0 to 1). Note that while a stoichiometry normalized to 4 O as above may be more familiar, the reaction to form such spinels is an oxidation reaction involving O_2, where it is the Co amount that remains constant. Hence, one could also write the formula unit above as $[Co^{II}_{1-y}]_{8a}[Li_{3y}]_{16c}[Co^{III}_{2+y}]_{16d}O_{4+2y}$. Although undetectable by XRD, the observation of an additional Raman band at low frequencies for samples at the edge of the $AB_2O_4 > A_2B_2O_4$ transition seems to validate such a hypothesis. To our knowledge, $[Co^{II}_{2(1-y)/(2+y)}]_T[Li_{6y/(2+y)}]_O[Co^{III}_2]_OO_4$ was only ever evidenced by transmission electron microscopy,[101] following speculations arising from Rietveld refinement of XRD data.

While we have clearly proven the existence of two spinel phases, the exact Li, Co stoichiometries of AB_2O_4 spinels and $A_2B_2O_4$ quasi-spinels crystallizing at different temperatures remain to be determined. While AB_2O_4-type spinel phases were detected as main polymorph(s) in both heated $Co(OH)_2$- and Co_3O_4-based blends from ϑ = 270 °C, one can still observe that the decrease in cell volume (lithiation) is reported earlier when using $Co(OH)_2$ as a precursor (ϑ = 290 °C), as opposed to Co_3O_4 (ϑ = 375 °C). A comparative evolution of cell volumes for cubic and layered phases formed out of both $Co(OH)_2$ and Co_3O_4 blends can be seen in Figure 10. The earlier onset of lithiation for the $Co(OH)_2$ blend is

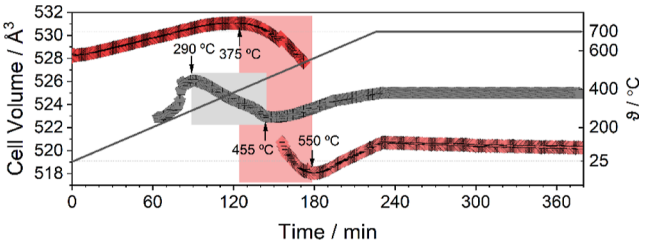

Figure 10. Comparative evolution of cell volumes for spinels (AB_2O_4 and $A_2B_2O_4$) formed from heat treatment of either $Co(OH)_2$/LiOH·H_2O (in gray) or Co_3O_4/LiOH·H_2O (in red). The shaded gray and red areas represent the main spinel lithiation temperature ranges for $Co(OH)_2$/LiOH·H_2O and Co_3O_4/LiOH·H_2O blends, respectively.

evident; nonetheless, the cell volumes reported at a given temperature for the cubic phases are significantly different. However, since line broadening was persistent in all patterns collected for the $Co(OH)_2$/LiOH·H_2O blend, the cell volumes reported here are grossly averaged, making it challenging to discuss any discrepancies that may arise from different Li, Co concentrations.

Overall, although similar spinel (AB_2O_4) or quasi-spinel ($A_2B_2O_4$) structures seem to be stabilized over the same temperature ranges when using Co_3O_4 or $Co(OH)_2$ as the precursor, their respective Li, Co stoichiometries may still largely differ at a given temperature. Additionally, samples prepared from $Co(OH)_2$ remained poorly crystallized throughout the whole heat treatment, as opposed to those from Co_3O_4. This can be considered as a significant kinetic advantage for the lithiation of the hydroxide-based Co precursor. While a dwell at 700 °C for several hours helped promote crystal growth for the final LCO powders, products prepared from Co_3O_4 still exhibited larger coherent domains. This should be taken into consideration when trying to synthesize both Co-based cathodes and cathode coatings. In fact, their electrochemical performance will strongly depend not only on the structure but also on the overall crystallinity and Li stoichiometry. The results described above, which could only be comprehensively obtained by the combined use of *in situ* XRD and *ex situ* Raman spectroscopy, can be used as a guide to select processing conditions for Co-based coatings for NCM materials, depending on the desired structure, morphology, and composition.

ASSOCIATED CONTENT

Supporting Information

The Supporting Information is available free of charge at https://pubs.acs.org/doi/10.1021/acs.chemmater.2c02050.

Simulated XRD patterns for various Li−Co−O compounds and mixtures thereof; contour plots of all XRD patterns collected during heating of the two precursor mixtures at a rate of 3 °C/min; analogous patterns but at a rate of 20 °C/min; Rietveld refinement profiles of structures fitted to the variable temperature *in situ* XRD data collected from the LiOH·H_2O + $Co(OH)_2$ blend; *ex situ* XRD patterns collected from samples used for

Raman spectroscopy prepared by heating the two mixtures of precursors; Rietveld refinement profiles of structures fitted to the variable temperature *in situ* XRD data collected from the $LiOH{\cdot}H_2O$ + Co_3O_4 blend; and refinement parameters (PDF)

AUTHOR INFORMATION

Corresponding Author

Matteo Bianchini − *Battery and Electrochemistry Laboratory, Institute of Nanotechnology, Karlsruhe Institute of Technology (KIT), 76344 Eggenstein-Leopoldshafen, Germany; BASF SE, 67056 Ludwigshafen, Germany; University of Bayreuth, Bavarian Center for Battery Technology (BayBatt), 95447 Bayreuth, Germany;* orcid.org/0000-0003-4034-7706; Email: matteo.bianchini@uni-bayreuth.de

Authors

Marie Duffiet − *Battery and Electrochemistry Laboratory, Institute of Nanotechnology, Karlsruhe Institute of Technology (KIT), 76344 Eggenstein-Leopoldshafen, Germany*

Damian Goonetilleke − *Battery and Electrochemistry Laboratory, Institute of Nanotechnology, Karlsruhe Institute of Technology (KIT), 76344 Eggenstein-Leopoldshafen, Germany;* orcid.org/0000-0003-1033-4787

François Fauth − *CELLS—ALBA Synchrotron, Cerdanyola del Vallès 08290 Barcelona, Spain;* orcid.org/0000-0001-9465-3106

Torsten Brezesinski − *Battery and Electrochemistry Laboratory, Institute of Nanotechnology, Karlsruhe Institute of Technology (KIT), 76344 Eggenstein-Leopoldshafen, Germany;* orcid.org/0000-0002-4336-263X

Jürgen Janek − *Battery and Electrochemistry Laboratory, Institute of Nanotechnology, Karlsruhe Institute of Technology (KIT), 76344 Eggenstein-Leopoldshafen, Germany; Institute of Physical Chemistry & Center for Materials Science (ZfM/LaMa), Justus-Liebig-University Giessen, 35392 Giessen, Germany;* orcid.org/0000-0002-9221-4756

Notes

The authors declare no competing financial interest.

ACKNOWLEDGMENTS

This work was supported by BASF SE. The authors acknowledge the ALBA synchrotron for the beamtime awarded under proposal 2020094478. Part of this work was undertaken at the MSPD beamline at ALBA synchrotron with the collaboration of ALBA staff and support from the project CALIPSOplus (grant 730872) under grant agreement 730872 from the EU Framework Programme for Research and Innovation HORIZON 2020.

REFERENCES

(1) Mizushima, K.; Jones, P. C.; Wiseman, P. J.; Goodenough, J. B. Li_xCoO_2 (0< x<1): A New Cathode Material for Batteries of High Energy Density. *Mater. Res. Bull.* **1980**, *15*, 783−789.

(2) Kikkawa, S.; Miyazaki, S.; Koizumi, M. Deintercalated $NaCoO_2$ and $LiCoO_2$. *J. Solid State Chem.* **1986**, *62*, 35−39.

(3) Wang, L.; Chen, B.; Ma, J.; Cui, G.; Chen, L. Reviving Lithium Cobalt Oxide-Based Lithium Secondary Batteries-toward a Higher Energy Density. *Chem. Soc. Rev.* **2018**, *47*, 6505−6602.

(4) Lyu, Y.; Wu, X.; Wang, K.; Feng, Z.; Cheng, T.; Liu, Y.; Wang, M.; Chen, R.; Xu, L.; Zhou, J.; Lu, Y.; Guo, B. An Overview on the Advances of $LiCoO_2$ Cathodes for Lithium-Ion Batteries. *Adv. Energy Mater.* **2021**, *11*, 2000982.

(5) Shikano, M.; Funahashi, R. Electrical and Thermal Properties of Single-Crystalline $(Ca_2CoO_3)_{0.7}CoO_2$ with a $Ca_3Co_4O_9$ Structure. *Appl. Phys. Lett.* **2003**, *82*, 1851−1853.

(6) Liu, Y.; Wang, W.; Yang, J.; Li, S. Recent Advances of Layered Thermoelectric Materials. *Adv. Sustainable Syst.* **2018**, *2*, 1800046.

(7) Schmidt-Szałowski, K.; Krawczyk, K.; Petryk, J. The Properties of Cobalt Oxide Catalyst for Ammonia Oxidation. *Appl. Catal., A* **1998**, *175*, 147−157.

(8) Liu, Y.-C.; Koza, J. A.; Switzer, J. A. Conversion of Electrodeposited $Co(OH)_2$ to CoOOH and Co_3O_4, and Comparison of Their Catalytic Activity for the Oxygen Evolution Reaction. *Electrochim. Acta* **2014**, *140*, 359−365.

(9) Takada, K.; Sakurai, H.; Takayama-Muromachi, E.; Izumi, F.; Dilanian, R. A.; Sasaki, T. Superconductivity in Two-Dimensional CoO_2 Layers. *Nature* **2003**, *422*, 53−55.

(10) Jagadale, A. D.; Kumbhar, V. S.; Dhawale, D. S.; Lokhande, C. D. Performance Evaluation of Symmetric Supercapacitor Based on Cobalt Hydroxide $[Co(OH)_2]$ Thin Film Electrodes. *Electrochim. Acta* **2013**, *98*, 32−38.

(11) Olchowka, J.; Tailliez, T.; Bourgeois, L.; Dourges, M.; Guerlou-Demourgues, L. Ionic Liquids to Monitor the Nano-Structuration and the Surface Functionalization of Material Electrodes: A Proof of Concept Applied to Cobalt Oxyhydroxide. *Nanoscale Adv.* **2019**, *1*, 2240−2249.

(12) Invernizzi, R.; Guerlou-Demourgues, L.; Weill, F.; Lemoine, A.; Dourges, M.-A.; Baraille, I.; Flahaut, D.; Olchowka, J. Controlled Nanostructuration of Cobalt Oxyhydroxide Electrode Material for Hybrid Supercapacitors. *Materials* **2021**, *14*, 2325.

(13) Kim, Y.; Cho, J. Lithium-Reactive $Co_3(PO_4)_2$ Nanoparticle Coating on High-Capacity $LiNi_{0.8}Co_{0.16}Al_{0.04}O_2$ Cathode Material for Lithium Rechargeable Batteries. *J. Electrochem. Soc.* **2007**, *154*, A495.

(14) Yan, X.; Chen, L.; Shah, S. A.; Liang, J.; Liu, Z. The Effect of Co_3O_4 & $LiCoO_2$ Cladding Layer on the High Rate and Storage Property of High Nickel Material $LiNi_{0.8}Co_{0.15}Al_{0.05}O_2$ by Simple One-Step Wet Coating Method. *Electrochim. Acta* **2017**, *249*, 179−188.

(15) Tao, F.; Yan, X.; Liu, J.-J.; Zhang, H.-L.; Chen, L. Effects of PVP-Assisted Co_3O_4 Coating on the Electrochemical and Storage Properties of $LiNi_{0.6}Co_{0.2}Mn_{0.2}O_2$ at High Cut-off Voltage. *Electrochim. Acta* **2016**, *210*, 548−556.

(16) Min, K.; Park, K.; Park, S. Y.; Seo, S.-W.; Choi, B.; Cho, E. Residual Li Reactive Coating with Co_3O_4 for Superior Electrochemical Properties of $LiNi_{0.91}Co_{0.06}Mn_{0.03}O_2$ Cathode Material. *J. Electrochem. Soc.* **2018**, *165*, A79−A85.

(17) Li, Y.; Deng, S.; Chen, Y.; Gao, J.; Zhu, J.; Xue, L.; Lei, T.; Cao, G.; Guo, J.; Wang, S. Dual Functions of Residue Li-Reactive Coating with $C_4H_6CoO_4$ on High-Performance $LiNiO_2$ Cathode Material. *Electrochim. Acta* **2019**, *300*, 26−35.

(18) Kim, Y.; Park, H.; Warner, J. H.; Manthiram, A. Unraveling the Intricacies of Residual Lithium in High-Ni Cathodes for Lithium-Ion Batteries. *ACS Energy Lett.* **2021**, *6*, 941−948.

(19) Huang, J.; Duan, J.; Du, K.; Cao, Y.; Peng, Z.; Hu, G. Enhanced Cycling Performance of $LiNi_{0.9}Co_{0.08}Al_{0.02}O_2$ via Co-Rich Surface. *JOM* **2020**, *72*, 738−744.

(20) Huang, Y.; Huang, Y.; Hu, X. Enhanced Electrochemical Performance of $LiNi_{0.8}Co_{0.15}Al_{0.05}O_2$ by Nanoscale Surface Modification with Co_3O_4. *Electrochim. Acta* **2017**, *231*, 294−299.

(21) Gummow, R. J.; Liles, D. C.; Thackeray, M. M.; David, W. I. F. A reinvestigation of the structures of lithium-cobalt-oxides with neutron-diffraction data. *Mater. Res. Bull.* **1993**, *28*, 1177−1184.

(22) Kan, Y.; Hu, Y.; Ren, Y.; Bareño, J.; Bloom, I.; Sun, Y.-K.; Amine, K.; Chen, Z. Differentiating Allotropic $LiCoO_2/Li_2Co_2O_4$: A

Structural and Electrochemical Study. *J. Power Sources* **2014**, *271*, 97−103.
(23) Tintignac, S.; Baddour-Hadjean, R.; Pereira-Ramos, J.-P.; Salot, R. High Performance Sputtered $LiCoO_2$ Thin Films Obtained at a Moderate Annealing Treatment Combined to a Bias Effect. *Electrochim. Acta* **2012**, *60*, 121−129.
(24) Huang, W.; Frech, R. Vibrational Spectroscopic and Electrochemical Studies of the Low and High Temperature Phases of $LiCo_{1-x}M_xO_2$ (M = Ni or Ti). *Solid State Ionics* **1996**, *86*−*88*, 395−400.
(25) Julien, C. Relationship Between Structure And Electrochemistry In Disordered $Licoo_2$ Cathode Materials. *Electrochem. Soc., Proc.* **2001**, *2000*, 11.
(26) Kim, S.; Hegde, V. I.; Yao, Z.; Lu, Z.; Amsler, M.; He, J.; Hao, S.; Croy, J. R.; Lee, E.; Thackeray, M. M.; Wolverton, C. First-Principles Study of Lithium Cobalt Spinel Oxides: Correlating Structure and Electrochemistry. *ACS Appl. Mater. Interfaces* **2018**, *10*, 13479−13490.
(27) Kim, J.; Fulmer, P.; Manthiram, A. Synthesis of $LiCoO_2$ Cathodes by an Oxidation Reaction in Solution and Their Electrochemical Properties. *Mater. Res. Bull.* **1999**, *34*, 571−579.
(28) Yang, Z.; Xing, G.; Yang, J.; Mao, C.; Du, J. Effect of Annealing Temperature on Structure and Electrochemical Properties of $LiCoO_2$ Cathode Thin Films. *Rare Met.* **2006**, *25*, 189−192.
(29) Han, C.-H.; Hong, Y.-S.; Park, C. M.; Kim, K. Synthesis and Electrochemical Properties of Lithium Cobalt Oxides Prepared by Molten-Salt Synthesis Using the Eutectic Mixture of $LiCl−Li_2CO_3$. *J. Power Sources* **2001**, *92*, 95−101.
(30) Imanishi, N.; Fujii, M.; Hirano, A.; Takeda, Y. Synthesis and characterization of nonstoichiometric $LiCoO_2$. *J. Power Sources* **2001**, *97*−*98*, 287−289.
(31) Imanishi, N.; Yamade, M.; Ichikawa, T.; Hirano, A.; Takeda, Y. Characterization and Electrode Behavior of Li_xCoO_2 (x>1). *Ionics* **2002**, *8*, 100−107.
(32) Levasseur, S.; Ménétrier, M.; Delmas, C. Combined Effects of Ni and Li Doping on the Phase Transitions in Li_xCoO_2. *J. Electrochem. Soc.* **2002**, *149*, A1533.
(33) Ménétrier, M.; Carlier, D.; Blangero, M.; Delmas, C. On "Really" Stoichiometric LiCoO2Electrochem. *Electrochem. Solid-State Lett.* **2008**, *11*, A179−A182.
(34) Duffiet, M.; Blangero, M.; Cabelguen, P.-E.; Delmas, C.; Carlier, D. Influence of the Initial Li/Co Ratio in $LiCoO_2$ on the High-Voltage Phase-Transitions Mechanisms. *J. Phys. Chem. Lett.* **2018**, *9*, 5334−5338.
(35) Gu, Y.; Chen, D.; Jiao, X. Synthesis and Electrochemical Properties of Nanostructured $LiCoO_2$ Fibers as Cathode Materials for Lithium-Ion Batteries. *J. Phys. Chem. B* **2005**, *109*, 17901−17906.
(36) Ying, J.; Jiang, C.; Wan, C. Preparation and Characterization of High-Density Spherical $LiCoO_2$ Cathode Material for Lithium Ion Batteries. *J. Power Sources* **2004**, *129*, 264−269.
(37) Xiao, X.; Yang, L.; Zhao, H.; Hu, Z.; Li, Y. Facile synthesis of $LiCoO_2$ nanowires with high electrochemical performance. *Nano Res.* **2012**, *5*, 27−32.
(38) Xiao, X.; Liu, X.; Wang, L.; Zhao, H.; Hu, Z.; He, X.; Li, Y. $LiCoO_2$ Nanoplates with Exposed (001) Planes and High Rate Capability for Lithium-Ion Batteries. *Nano Res.* **2012**, *5*, 395−401.
(39) Antolini, E. $LiCoO_2$: Formation, Structure, Lithium and Oxygen Nonstoichiometry, Electrochemical Behaviour and Transport Properties. *Solid State Ionics* **2004**, *170*, 159−171.
(40) Wicker, S. A.; Walker, E. H. Revisited: Decomposition or Melting? Formation Mechanism Investigation of $LiCoO_2$ via In-Situ Time-Resolved X-Ray Diffraction. *Inorg. Chem.* **2013**, *52*, 1772−1779.
(41) Gim, J.; Zhang, Y.; Gao, H.; Xu, G.-L.; Guo, F.; Ren, Y.; Amine, K.; Chen, Z. Probing Solid-State Reaction through Microstrain: A Case Study on Synthesis of $LiCoO_2$. *J. Power Sources* **2020**, *469*, 228422.
(42) Jensen, K. M. Ø.; Tyrsted, C.; Bremholm, M.; Iversen, B. B. In Situ Studies of Solvothermal Synthesis of Energy Materials. *ChemSusChem* **2014**, *7*, 1594−1611.
(43) Rao, R. P.; Gu, W.; Sharma, N.; Peterson, V. K.; Avdeev, M.; Adams, S. In Situ Neutron Diffraction Monitoring of $Li_7La_3Zr_2O_{12}$ Formation: Toward a Rational Synthesis of Garnet Solid Electrolytes. *Chem. Mater.* **2015**, *27*, 2903−2910.
(44) Duffiet, M.Investigation of Structural Failure Mechanisms of $LiCoO_2$ at High Voltage and Material Optimization through Aluminum Doping. Ph.D. Thesis, Université de Bordeaux, 2019.
(45) Bianchini, M.; Fauth, F.; Hartmann, P.; Brezesinski, T.; Janek, J. An in situ structural study on the synthesis and decomposition of $LiNiO_2$. *J. Mater. Chem. A* **2020**, *8*, 1808−1820.
(46) Bianchini, M.; Wang, J.; Clément, R. J.; Ouyang, B.; Xiao, P.; Kitchaev, D.; Shi, T.; Zhang, Y.; Wang, Y.; Kim, H.; Zhang, M.; Bai, J.; Wang, F.; Sun, W.; Ceder, G. The Interplay between Thermodynamics and Kinetics in the Solid-State Synthesis of Layered Oxides. *Nat. Mater.* **2020**, *19*, 1088−1095.
(47) Bai, J.; Sun, W.; Zhao, J.; Wang, D.; Xiao, P.; Ko, J. Y. P.; Huq, A.; Ceder, G.; Wang, F. Kinetic Pathways Templated by Low-Temperature Intermediates during Solid-State Synthesis of Layered Oxides. *Chem. Mater.* **2020**, *32*, 9906−9913.
(48) Giorgi, L.; Carewska, M.; Patriarca, M.; Scaccia, S.; Simonetti, E.; Di Bartolomeo, A. Development and Characterization of Novel Cathode Materials for Molten Carbonate Fuel Cell. *J. Power Sources* **1994**, *49*, 227−243.
(49) Lundblad, A.; Bergman, B. Synthesis of $LiCoO_2$ Starting from Carbonate Precursors I. The Reaction Mechanisms. *Solid State Ionics* **1997**, *96*, 173−181.
(50) Levasseur, S.Contribution à l'étude Des Phases $Li_x(Co, M)O_2$ En Tant Que Matériaux d'électrode Positive Des Batteries Li-Ion. Effets Combinés de La Surstoechiométrie En Lithium et de La Substitution (M= Ni, Mg). Ph.D. Thesis, Université Sciences et Technologies-Bordeaux I, 2001.
(51) Reimers, J. N.; Li, W.; Rossen, E.; Dahn, J. R. Structure, Diffraction and Energetic Stability of the Spinel Form of $LiCoO_2$. *MRS Proc.* **1992**, *293*, 3.
(52) Gummow, R.; Liles, D.; Thackeray, M.; David, W. A Reinvestigation of the Structures of Lithium-Cobalt-Oxides with Neutron-Diffraction Data. *Mater. Res. Bull.* **1993**, *28*, 1177−1184.
(53) Maiyalagan, T.; Jarvis, K. A.; Therese, S.; Ferreira, P. J.; Manthiram, A. Spinel-Type Lithium Cobalt Oxide as a Bifunctional Electrocatalyst for the Oxygen Evolution and Oxygen Reduction Reactions. *Nat. Commun.* **2014**, *5*, 3949.
(54) Inaba, M.; Iriyama, Y.; Ogumi, Z.; Todzuka, Y.; Tasaka, A. Raman Study of Layered Rock-Salt $LiCoO_2$ and Its Electrochemical Lithium Deintercalation. *J. Raman Spectrosc.* **1997**, *28*, 613−617.
(55) Novák, P.; Panitz, J.-C.; Joho, F.; Lanz, M.; Imhof, R.; Coluccia, M. Advanced in Situ Methods for the Characterization of Practical Electrodes in Lithium-Ion Batteries. *J. Power Sources* **2000**, *90*, 52−58.
(56) Nishi, T.; Nakai, H.; Kita, A. Visualization of the State-of-Charge Distribution in a $LiCoO_2$ Cathode by In Situ Raman Imaging. *J. Electrochem. Soc.* **2013**, *160*, A1785.
(57) Gross, T.; Hess, C. Raman diagnostics of $LiCoO_2$ electrodes for lithium-ion batteries. *J. Power Sources* **2014**, *256*, 220−225.
(58) Snyder, C.; Apblett, C.; Grillet, A.; Beechem, T.; Duquette, D. Measuring Li^+ Inventory Losses in $LiCoO_2$ /Graphite Cells Using Raman Microscopy. *J. Electrochem. Soc.* **2016**, *163*, A1036−A1041.
(59) Matsuda, Y.; Kuwata, N.; Okawa, T.; Dorai, A.; Kamishima, O.; Kawamura, J. In Situ Raman Spectroscopy of Li_xCoO_2 Cathode in Li/Li_3PO_4/$LiCoO_2$ All-Solid-State Thin-Film Lithium Battery. *Solid State Ionics* **2019**, *335*, 7−14.
(60) Fauth, F.; Peral, I.; Popescu, C.; Knapp, M. The New Material Science Powder Diffraction Beamline at ALBA Synchrotron. *Powder Diffr.* **2013**, *28*, S360−S370.
(61) Chupas, P. J.; Chapman, K. W.; Kurtz, C.; Hanson, J. C.; Lee, P. L.; Grey, C. P. A Versatile Sample-Environment Cell for Non-Ambient X-Ray Scattering Experiments. *J. Appl. Crystallogr.* **2008**, *41*, 822−824.
(62) Toby, B. H.; Von Dreele, R. B. GSAS-II: The Genesis of a Modern Open-Source All Purpose Crystallography Software Package. *J. Appl. Crystallogr.* **2013**, *46*, 544−549.

(63) Pauporté, T.; Mendoza, L.; Cassir, M.; Bernard, M. C.; Chivot, J. Direct Low-Temperature Deposition of Crystallized CoOOH Films by Potentiostatic Electrolysis. *J. Electrochem. Soc.* **2005**, *152*, C49.
(64) Ravindra, A. V.; Behera, B. C.; Padhan, P. Laser Induced Structural Phase Transformation of Cobalt Oxides Nanostructures. *J. Nanosci. Nanotechnol.* **2014**, *14*, 5591−5595.
(65) Rivas-Murias, B.; Salgueiriño, V. Thermodynamic CoO−Co_3O_4 Crossover Using Raman Spectroscopy in Magnetic Octahedron-Shaped Nanocrystals. *J. Raman Spectrosc.* **2017**, *48*, 837−841.
(66) Hunt, D.; Garbarino, G.; Rodríguez-Velamazán, J.; Ferrari, V.; Jobbagy, M.; Scherlis, A. The magnetic structure of β-cobalt hydroxide and the effect of spin-orientation. *Phys. Chem. Chem. Phys.* **2016**, *18*, 30407−30414.
(67) Mockenhaupt, C.; Zeiske, T.; Lutz, H. D. Crystal Structure of Brucite-Type Cobalt Hydroxide β-Co$\{O(H,D)\}_2$ — Neutron Diffraction, IR and Raman Spectroscopy. *J. Mol. Struct.* **1998**, *443*, 191−196.
(68) Lutz, H. D.; Möller, H.; Schmidt, M. Lattice Vibration Spectra. Part LXXXII. Brucite-Type Hydroxides $M(OH)_2$ (M = Ca, Mn, Co, Fe, Cd) — IR and Raman Spectra, Neutron Diffraction of $Fe(OH)_2$. *J. Mol. Struct.* **1994**, *328*, 121−132.
(69) Shieh, S. R.; Duffy, T. S. Raman Spectroscopy of $Co(OH)_2$ at High Pressures: Implications for Amorphization and Hydrogen Repulsion. *Phys. Rev. B: Condens. Matter Mater. Phys.* **2002**, *66*, 134301.
(70) Delaplane, R. G.; Ibers, J. A.; Ferraro, J. R.; Rush, J. J. Diffraction and Spectroscopic Studies of the Cobaltic Acid System $HCoC_2$−$DCoO_2$. *J. Chem. Phys.* **1969**, *50*, 1920−1927.
(71) Yang, J.; Liu, H.; Martens, W. N.; Frost, R. L. Synthesis and Characterization of Cobalt Hydroxide, Cobalt Oxyhydroxide, and Cobalt Oxide Nanodiscs. *J. Phys. Chem. C* **2010**, *114*, 111−119.
(72) Upadhyay, D.; Pratap, A.; Jha, P. K. A First Principles Study on Structural, Dynamical, and Mechanical Stability of Newly Predicted Delafossite $HCoO_2$ at High Pressure. *J. Raman Spectrosc.* **2019**, *50*, 603−613.
(73) Guo, B.; Li, T.; Hu, H. Anodic Deposition of CoOOH Films with Excellent Performance for Electrochemical Capacitors. *J. Appl. Electrochem.* **2016**, *46*, 403−421.
(74) Guo, B.; Li, T.; Liu, H.; Xie, R.; Zhang, X.; Huang, H.; Li, Y.; Ma, Y.; Huo, J. Fabrication, Structure, Electrochemical Properties, and Enhanced Pseudocapacitive Performance of Cobalt Oxyhydroxide Films via a Simple Strategy. *Ionics* **2020**, *26*, 423−439.
(75) Yang, J.; Sasaki, T. Synthesis of CoOOH Hierarchically Hollow Spheres by Nanorod Self-Assembly through Bubble Templating. *Chem. Mater.* **2008**, *20*, 2049−2056.
(76) Deliens, M.; Goethals, H. Polytypism of Heterogenite. *Mineral. Mag.* **1973**, *39*, 152−157.
(77) Knop, O.; Reid, K. I. G.; Sutarno; Nakagawa, Y. Chalkogenides of the Transition Elements. VI. X-Ray, Neutron, and Magnetic Investigation of the Spinels Co_3O_4, $NiCo_2O_4$, Co_3S_4, and $NiCo_2S_4$. *Can. J. Chem.* **1968**, *46*, 3463−3476.
(78) White, W. B.; DeAngelis, B. A. Interpretation of the Vibrational Spectra of Spinels. *Spectrochim. Acta, Part A* **1967**, *23*, 985−995.
(79) Bai, L.; Pravica, M.; Zhao, Y.; Park, C.; Meng, Y.; Sinogeikin, S. V.; Shen, G. Charge Transfer in Spinel Co_3O_4 at High Pressures. *J. Phys.: Condens. Matter* **2012**, *24*, 435401.
(80) Hadjiev, V. G.; Iliev, M. N.; Vergilov, I. V. The Raman Spectra of Co_3O_4. *J. Phys. C: Solid State Phys.* **1988**, *21*, L199−L201.
(81) Lorite, I.; Romero, J. J.; Fernández, J. F. Effects of the Agglomeration State on the Raman Properties of Co_3O_4 Nanoparticles. *J. Raman Spectrosc.* **2012**, *43*, 1443−1448.
(82) Burba, C. M.; Shaju, K. M.; Bruce, P. G.; Frech, R. Infrared and Raman Spectroscopy of Nanostructured LT-$LiCoO_2$ Cathodes for Li-Ion Rechargeable Batteries. *Vib. Spectrosc.* **2009**, *51*, 248−250.
(83) Mendoza, L.; Baddour-Hadjean, R.; Cassir, M.; Pereira-Ramos, J. P. Raman Evidence of the Formation of LT-$LiCoO_2$ Thin Layers on NiO in Molten Carbonate at 650°C. *Appl. Surf. Sci.* **2004**, *225*, 356−361.
(84) Porthault, H.; Baddour-Hadjean, R.; Le Cras, F.; Bourbon, C.; Franger, S. Raman Study of the Spinel-to-Layered Phase Transformation in Sol−Gel $LiCoO_2$ Cathode Powders as a Function of the Post-Annealing Temperature. *Vib. Spectrosc.* **2012**, *62*, 152−158.
(85) Fu, J.; Bai, Y.; Liu, C.; Yu, H.; Mo, Y. Physical Characteristic Study of $LiCoO_2$ Prepared by Molten Salt Synthesis Method in 550−800°C. *Mater. Chem. Phys.* **2009**, *115*, 105−109.
(86) Akimoto, J.; Gotoh, Y.; Oosawa, Y. Synthesis and Structure Refinement of $LiCoO_2$ Single Crystals. *J. Solid State Chem.* **1998**, *141*, 298−302.
(87) Wang, X.; Loa, I.; Kunc, K.; Syassen, K.; Amboage, M. Effect of Pressure on the Structural Properties and Raman Modes of $LiCoO_2$. *Phys. Rev. B: Condens. Matter Mater. Phys.* **2005**, *72*, 224102.
(88) Bookin, A. S.; Drits, V. A. Polytype Diversity of the Hydrotalcite-Like Minerals I. Possible Polytypes and Their Diffraction Features. *Clays Clay Miner.* **1993**, *41*, 551−557.
(89) Tang, C.-W.; Wang, C.-B.; Chien, S.-H. Characterization of Cobalt Oxides Studied by FT-IR, Raman, TPR and TG-MS. *Thermochim. Acta* **2008**, *473*, 68−73.
(90) Bardé, F.; Palacin, M.-R.; Beaudoin, B.; Delahaye-Vidal, A.; Tarascon, J.-M. New Approaches for Synthesizing ΓIII-CoOOH by Soft Chemistry. *Chem. Mater.* **2004**, *16*, 299−306.
(91) Butel, M.; Gautier, L.; Delmas, C. Cobalt Oxyhydroxides Obtained by "Chimie Douce" Reactions: Structure and Electronic Conductivity Properties. *Solid State Ionics* **1999**, *122*, 271−284.
(92) Ramesh, T. N. Investigation on the Oxidation Mechanism of Cobalt Hydroxide to Cobalt Oxyhydroxide. *Ind. Eng. Chem. Res.* **2010**, *49*, 1530−1533.
(93) Kudielka, A.; Bette, S.; Dinnebier, R. E.; Abeykoon, M.; Pietzonka, C.; Harbrecht, B. Variability of Composition and Structural Disorder of Nanocrystalline CoOOH Materials. *J. Mater. Chem. C* **2017**, *5*, 2899−2909.
(94) Amatucci, G. G.; Tarascon, J. M.; Larcher, D.; Klein, L. C. Synthesis of Electrochemically Active $LiCoO_2$ and $LiNiO_2$ at 100 °C. *Solid State Ionics* **1996**, *84*, 169−180.
(95) Larcher, D.; Palacín, M. R.; Amatucci, G. G.; Tarascon, J. -M. Electrochemically Active $LiCoO_2$ and $LiNiO_2$ Made by Cationic Exchange under Hydrothermal Conditions. *J. Electrochem. Soc.* **1997**, *144*, 408−417.
(96) Gummow, R. J.; Thackeray, M. M. Characterization of LT-$Li_xCo_{1-y}Ni_yO_2$ Electrodes for Rechargeable Lithium Cells. *J. Electrochem. Soc.* **1993**, *140*, 3365−3368.
(97) Rossen, E.; Reimers, J.; Dahn, J. Synthesis and Electrochemistry of Spinel LT-$LiCoO_2$. *Solid State Ionics* **1993**, *62*, 53−60.
(98) Antaya, M.; Cearns, K.; Preston, J. S.; Reimers, J. N.; Dahn, J. R. In Situ Growth of Layered, Spinel, and Rock-salt $LiCoO_2$ by Laser Ablation Deposition. *J. Appl. Phys.* **1994**, *76*, 2799−2806.
(99) Garcia, B.; Farcy, J.; Pereira-Ramos, J. P.; Baffier, N. Electrochemical Properties of Low Temperature Crystallized $LiCoO_2$. *J. Electrochem. Soc.* **1997**, *144*, 1179−1184.
(100) Shao-Horn, Y.; Hackney, S. A.; Johnson, C. S.; Kahaian, A. J.; Thackeray, M. M. Structural Features of Low-Temperature $LiCoO_2$ and Acid-Delithiated Products. *J. Solid State Chem.* **1998**, *140*, 116−127.
(101) Shao-Horn, Y.; Hackney, S. A.; Kahaian, A. J.; Thackeray, M. M. Structural Stability of $LiCoO_2$ at 400°C. *J. Solid State Chem.* **2002**, *168*, 60−68.
(102) Choi, S.; Manthiram, A. Chemical Synthesis and Properties of Spinel $Li_{1-x}Co_2O_{4-\delta}$. *J. Solid State Chem.* **2002**, *164*, 332−338.
(103) Choi, S.; Manthiram, A.Synthesis and Electrochemical Properties of Spinel $LiCo_2O_4$ Cathodes. *Materials for Electrochemical Energy Conversion and Storage*; John Wiley & Sons, Ltd, 2006; pp 215−224.
(104) Appandairajan, N. K.; Viswanathan, B.; Gopalakrishnan, J. Lithium-Substituted Cobalt Oxide Spinels $Li_xM_{1-x}Co_2O_4$ (M = Co^{2+}, Zn^{2+}; $0 \leq x \leq 0.4$). *J. Solid State Chem.* **1981**, *40*, 117−121.
(105) Zhecheva, E.; Stoyanova, R.; Angelov, S. Doping of Co_3O_4 with Lithium by a Solid-State Reaction in Air I. Oxidation Degree and Coordination of Cations. *Mater. Chem. Phys.* **1990**, *25*, 351−360.

(106) Zhecheva, E.; Stoyanova, R.; Angelov, S. Doping of Co_3O_4 with Lithium by a Solid State Reaction in Air II. Distribution of Lithium in the Solid Solution. *Mater. Chem. Phys.* **1990**, *25*, 361−373.
(107) Meza, E.; Alburquenque, D.; Ortiz, J.; Gautier, J. L. Lithium Cobalt Spinel Oxide: A Structural And Electrochemical Study. *J. Chil. Chem. Soc.* **2008**, *53*, 1494−1497.
(108) Liu, X.; Yi, R.; Zhang, N.; Shi, R.; Li, X.; Qiu, G. Cobalt Hydroxide Nanosheets and Their Thermal Decomposition to Cobalt Oxide Nanorings. *Chem.—Asian J.* **2008**, *3*, 732−738.
(109) Koza, J. A.; Hull, C. M.; Liu, Y.-C.; Switzer, J. A. Deposition of β-$Co(OH)_2$ Films by Electrochemical Reduction of Tris-(Ethylenediamine)Cobalt(III) in Alkaline Solution. *Chem. Mater.* **2013**, *25*, 1922−1926.
(110) Goodenough, J. B.; Wickham, D. G.; Croft, W. J. Some Magnetic and Crystallographic Properties of the System $Li^{+}_{x}Ni^{++}_{1-2x}Ni^{+++}_{x}O$. *J. Phys. Chem. Solids* **1958**, *5*, 107−116.
(111) Antolini, E. $Li_xNi_{1-x}O$ ($0<x\leq0.3$) Solid Solutions: Formation, Structure and Transport Properties. *Mater. Chem. Phys.* **2003**, *82*, 937−948.
(112) Chen, B.; Ben, L.; Yu, H.; Chen, Y.; Huang, X. Understanding Surface Structural Stabilization of the High-Temperature and High-Voltage Cycling Performance of Al^{3+}-Modified $LiMn_2O_4$ Cathode Material. *ACS Appl. Mater. Interfaces* **2018**, *10*, 550−559.
(113) Jayatissa, A. H.; Guo, K.; Jayasuriya, A. C.; Gupta, T. Fabrication of Nanocrystalline Cobalt Oxide via Sol−Gel Coating. *Mater. Sci. Eng. B* **2007**, *144*, 69−72.
(114) Julien, C.; Nazri, G. A.; Rougier, A. Electrochemical Performances of Layered $LiM_{1-y}M'_yO_2$ (M= Ni, Co; M′= Mg, Al, B) Oxides in Lithium Batteries. *Solid State Ionics* **2000**, *135*, 121−130.
(115) Fan, L.; Tang, D.; Wang, D.; Wang, Z.; Chen, L. $LiCoO_2$-Catalyzed Electrochemical Oxidation of Li_2CO_3. *Nano Res.* **2016**, *9*, 3903−3913.
(116) Kushida, K.; Kuriyama, K. Optical Absorption Related to Co-3d Bands in Sol−Gel Grown $LiCoO_2$ Films. *Solid State Commun.* **2001**, *118*, 615−618.
(117) Liu, H. L.; Ou-Yang, T. Y.; Tsai, H. H.; Lin, P. A.; Jeng, H. T.; Shu, G. J.; Chou, F. C. Electronic Structure and Lattice Dynamics of Li_xCoO_2 Single Crystals. *New J. Phys.* **2015**, *17*, 103004.
(118) Preudhomme, J.; Tarte, P. Infrared studies of spinels-II. *Spectrochim. Acta, Part A* **1971**, *27*, 845−851.
(119) Chang, I. F.; Mitra, S. S. Long Wavelength Optical Phonons in Mixed Crystals. *Adv. Phys.* **1971**, *20*, 359−404.
(120) Julien, C.; Massot, M.; Pérez-Vicente, C. Structural and Vibrational Studies of $LiNi_{1-y}Co_yVO_4$ ($0\leq y\leq1$) Cathodes Materials for Li-Ion Batteries. *Mater. Sci. Eng. B* **2000**, *75*, 6−12.
(121) Julien, C. M.; Massot, M. Raman Spectroscopic Studies of Lithium Manganates with Spinel Structure. *J. Phys.: Condens. Matter* **2003**, *15*, 3151−3162.
(122) Hosterman, B.Raman Spectroscopic Study of Solid Solution Spinel Oxides. Ph.D. Thesis, University of Nevada, Las Vegas, 2011.
(123) Verble, J. Temperature-Dependent Light-Scattering Studies of the Verwey Transition and Electronic Disorder in Magnetite. *Phys. Rev. B: Solid State* **1974**, *9*, 5236−5248.
(124) Yamanaka, T.; Ishii, M. Raman Scattering and Lattice Vibrations of Ni_2SiO_4 Spinel at Elevated Temperature. *Phys. Chem. Miner.* **1986**, *13*, 156−160.
(125) Cynn, H.; Sharma, S. K.; Cooney, T. F.; Nicol, M. High-Temperature Raman Investigation of Order-Disorder Behavior in the $MgAl_2O_4$ Spinel. *Phys. Rev. B: Condens. Matter Mater. Phys.* **1992**, *45*, 500−502.